Title

Periportal macrophages protect against commensal-driven liver inflammation

Authors

Yu Miyamoto[1,2,3], Junichi Kikuta[1,2,3,4], Takahiro Matsui[1,5], Tetsuo Hasegawa[1], Kentaro Fujii[1,2,3], Daisuke Okuzaki[2,6], Yu-chen Liu[2,6], Takuya Yoshioka[7], Shigeto Seno[8], Daisuke Motooka[2,6], Yutaka Uchida[1,2,3,4], Erika Yamashita[1,2,3], Shogo Kobayashi[9], Hidetoshi Eguchi[9], Eiichi Morii[5], Karl Tryggvason[10], Takashi Shichita[11], Hisako Kayama[2,12], Koji Atarashi[13], Jun Kunisawa[7], Kenya Honda[13], Kiyoshi Takeda[2,12], and Masaru Ishii[1,2,3,4*]

Affiliations

[1]Department of Immunology and Cell Biology, Graduate School of Medicine and Frontier Biosciences, Osaka University, Osaka, Japan

[2]WPI-Immunology Frontier Research Center, Osaka University, Osaka, Japan

[3]Life-omics Research Division, Institute for Open and Transdisciplinary Research Initiative, Osaka University, Osaka, Japan

[4]Laboratory of Bioimaging and Drug Discovery, National Institutes of Biomedical Innovation, Health and Nutrition, Osaka, Japan

[5]Department of Pathology, Graduate School of Medicine, Osaka University, Osaka, Japan

[6]Genome Information Research Center, Research Institute for Microbial Diseases, Osaka University, Osaka, Japan

[7]Laboratory of Vaccine Materials, Center for Vaccine and Adjuvant Research, National Institutes of Biomedical Innovation, Health and Nutrition, Osaka, Japan

[8]Department of Bioinformatic Engineering, Graduate School of Information Science and Technology, Osaka University, Osaka, Japan

[9]Department of Gastroenterological Surgery, Graduate School of Medicine, Osaka University, Osaka, Japan

[10]Cardiovascular & Metabolic Disorders Program, Duke-NUS, Duke-NUS Medical School, Singapore, Singapore

[11]Laboratory for Neuroinflammation and Repair, Medical Research Institute, Tokyo Medical and Dental University, Tokyo, Japan

[12]Department of Microbiology and Immunology, Graduate School of Medicine, Osaka University, Osaka, Japan

[13]Department of Microbiology and Immunology, School of Medicine, Keio University, Tokyo, Japan

***Corresponding Author:**

Masaru Ishii, Department of Immunology and Cell Biology, Graduate School of Medicine and Frontier Biosciences, Osaka University, 2-2 Yamada-oka, Suita, Osaka 565-0871, Japan

Tel: +81-6-6879-3880, Fax: +81-6-6879-3889, E-mail: mishii@icb.med.osaka-u.ac.jp

Abstract

The liver is the main gateway from the gut, and the unidirectional sinusoidal flow from portal to central veins constitutes heterogenous zones, including the periportal vein (PV) and pericentral vein zones[1–5]; however, functional differences in the immune system in each zone remain poorly understood. Here, intravital imaging revealed that inflammatory responses were suppressed in PV zones. The zone-specific single-cell transcriptomics detected an immunosuppressive macrophage subset enriched in PV zones that highly expresses IL-10 and Marco, a scavenger receptor sequestering pro-inflammatory PAMPs/DAMPs, and consequently suppressing immune responses. Induction of the Marco$^+$ immunosuppressive macrophages depended on gut microbiota, and especially, a specific bacterial family, Odoribacteraceae, was identified to induce this macrophage subset via its postbiotic, isoallo-lithocholic acid. Intestinal barrier leakage results in inflammation in PV zones, which was markedly augmented by Marco-deficient conditions. Chronic liver inflammatory diseases such as primary sclerosing cholangitis (PSC) and non-alcoholic steatohepatitis (NASH) showed decreased Marco$^+$ macrophages. Functional ablation of Marco$^+$ macrophages led to PSC-like inflammatory phenotypes related to colitis and exacerbated steatosis in NASH in animal experimental models. Collectively, commensal bacteria induce Marco$^+$ immunosuppressive macrophages, consequently limiting excessive inflammation at the gateway. Failure of this self-limiting

system promotes hepatic inflammatory disorders such as PSC and NASH.

Main text

The mammalian liver comprises repetitive hexagonal units called lobules in which blood flows unidirectionally from portal veins and hepatic arteries towards draining central veins. This polarised blood flow creates concentration gradients along the portal-central axis for blood substances, such as nutrients and oxygen, as well as physiologically active substances[1,2]. Based on this polarised liver structure, several reports have demonstrated the polarised functions of the periportal vein (PV) and pericentral vein (CV) zones. For example, hepatocytes in PV zones contribute to gluconeogenesis and cholesterol biosynthesis, whereas those in CV zones are involved in glutamine and bile acid production[3–5]. Liver sinusoidal endothelial cells (LSECs) produce different chemokines depending on their zonal location, which may guide the positioning of each immune cell type in the tissue[6,7]. In addition, hepatic stellate cells (HSCs) and LSECs in CV zones are prone to pathological changes upon exposure to carbon tetrachloride, thereby exhibiting overproduction of pathogenic collagens compared to those in PV zones[7,8]. The hepatic immune system consists of an asymmetric distribution of resident immune cells, especially Kupffer cells (resident macrophages), with a greater density around the portal veins[6,9], effectively preventing gut bacteria from entering the systemic circulation[6]. Nevertheless, the spatial heterogeneity in hepatic immune functions has not yet been explored.

In this study, we first performed spatial transcriptomic analysis of murine liver specimens, focusing on the immune/inflammatory system. We could distinguish between PV and CV zones

based on the specific expression of *Cyp2f2* and *Cyp2e1*, well-defined zonation markers for hepatocytes in PV and CV zones, respectively[10] (**Fig. 1a**), enabling the extraction of differentially expressed genes in each zone. We then performed the Gene Ontology analysis and selected immunity-related terms for detailed analysis. Periportally enriched immune pathways included many processes involved in the negative regulation of the immune system (**Fig. 1b**). This result suggested that immune/inflammatory responses are more repressed in PV than in CV zones. To directly visualise immune responses in PV and CV zones respectively, we used high-resolution intravital two-photon microscopy to assess the in situ behaviours of locally activated inflammatory cells highly expressing lysozyme M-GFP (LysM-GFP), mainly including neutrophils in the liver, using a laser damage-induced sterile inflammation model. These experiments revealed that neutrophils preferentially accumulated at damage sites in CV zones compared with those in PV zones (**Fig. 1c (top), 1d (left), Supplementary Video 1**). Even in the steady-state liver, neutrophils were inclined to reside in CV zones than in PV zones (**Extended Data Fig. 1, Supplementary Video 2**). Subsequently, we focused on the possible role of resident macrophages in the spatial heterogeneity of inflammatory responses in PV/CV zones. We intravenously administered clodronate liposomes (CLL) which specifically depleted the resident macrophages but not the other phagocytic myeloid cells (**Supplementary Fig. 1a, b**). We confirmed that CLL treatment did not alter the expression of most chemokines involved in neutrophil recruitment and did not increase the neutrophil infiltration (**Supplementary Fig.**

1b, c). Once resident macrophages were depleted by CLL (in the resident mac-depleted group), neutrophils were shown to be accumulated equally at damage sites in both PV and CV zones (**Fig. 1c (bottom), 1d (right), Supplementary Video 3**). We also examined the in situ behaviours of CX_3CR1-positive circulating monocytes/macrophages upon the laser-induced tissue damages[11]. We found their skewed accumulation in CV zones, similar to the case with neutrophils (**Extended Data Fig. 2a-c**), which was cancelled by depleting resident macrophages with CLL treatment (**Extended Data Fig. 2d,e**). These results suggest that periportal resident macrophages suppress inflammatory responses, with a greater inhibitory activity in PV zones.

To identify the immunosuppressive macrophage subset residing in PV zones, we developed a novel method for collecting liver-resident immune cells based on their locational information (*i.e.*, in PV or CV zones) using transgenic mice globally expressing photoactivatable-GFP (PA-GFP) (**Fig. 1e, Supplementary Fig. 2a**). After in vivo staining with a phycoerythrin (PE)-conjugated anti-E-cadherin antibody to demarcate PV zones[6], the livers were excised and freshly sectioned, followed by photoactivation in either the PV or CV zones using violet laser under microscopic guidance. Photoactivated (GFP^+) $CD45^+$ immune cells were collected for single-cell RNA sequencing, which provided single-cell transcriptomic data for 1,282 cells from PV zones and 1,179 cells from CV zones, including all immune cell types in the murine liver[9,12] (**Fig. 1f, Supplementary Fig. 2b, c**). Kupffer cells (liver resident macrophages) are

characterised by the expression of *Adgre1* and *Clec4f* (coding F4/80 and CLEC4F, respectively)[13] (**Supplementary Fig. 2c, d**). Among the different immune cell types in the liver, Kupffer cells can be further divided into at least two subpopulations based on their expression patterns, tentatively termed 'MP1' and 'MP2'. *Marco*, a class A scavenger receptor, was found to be exclusively expressed in the MP2 population (**Fig. 1g, Supplementary Fig. 3**). Additionally, typical anti-inflammatory cytokines, such as *Il10*, *Il1rn*, and *Tgfb1* were shown to be elevated in MP2, indicating the immunosuppressive property of MP2 (**Fig. 1h**). To investigate the spatial distributions of MP1/MP2 in each zone, we calculated a localisation score defined as the ratio of the number of PV zone-derived cells to that of CV zone-derived cells of a given subset: > 1 and < 1 indicate bias towards PV and CV zones, respectively (**Fig. 1f**). MP2 cells were substantially biased towards PV zones, whereas MP1 cells were biased towards CV zones. Immunofluorescence staining ensured that $Marco^{+}$ $F4/80^{+}$ cells (MP2) were exclusively concentrated in E-$cadherin^{+}$ PV zones; however, $Marco^{-}$ $F4/80^{+}$ cells (MP1) were equally scattered across the tissue (**Fig. 1i**). Additionally, we could validate the polarised distribution of neutrophils in CV zones observed using histological analyses (**Extended Data Fig. 1**) and confirmed the previous results representing periportal distribution of natural killer T cells (NKT), CX_3CR1-expressing macrophages and T cells[6,14]. The spatial transcriptomic analysis also verified periportally polarised expression of the anti-inflammatory molecules, *Il10*, *Il1rn*, and *Tgfb1*, which should be expressed in MP2 (**Supplementary Fig. 2e**).

77 Reanalyses of public murine datasets from the liver cell atlas[9] (large-scale single-cell and
78 spatial transcriptomic data) could detect the presence and skewed distribution of Marco$^+$ IL10$^+$
79 MP2 population (**Extended Data Fig. 3a-d**). Furthermore, based on the reanalyses of public
80 human single-cell transcriptomic database[15], *MARCO*- and *IL10*-expressing macrophage
81 subset could also be detected in the human liver, which should correspond to human MP2
82 (**Extended Data Fig. 3e, f**). This human MP2-like population was shown to be significantly
83 reduced in pathological conditions such as liver cirrhosis[15] (**Extended Data Fig. 3g**). The
84 presence of human MP2 would be further supported by a previous report describing periportal
85 MARCO$^+$ 'non-inflammatory' macrophages in the human liver[16]. These reanalyses of public
86 databases demonstrate that Marco$^+$ immunosuppressive macrophages are commonly present in
87 peri-portal vein regions in mice and humans.
88 Next, we examined the molecular mechanisms underlying the immunosuppressive action
89 of MP2 by focusing on interleukin-10 (IL-10) and Marco. Comparative quantification of *Il10*
90 expression in all the immune and non-immune cell types revealed that MP2 was the major IL-
91 10 producer in the liver (**Fig. 2a, b**). We validated the increased transcriptional activity of *Il10*
92 in MP2 compared to that in MP1 using *Il10*-Venus reporter mice (**Extended Data Fig. 4a**). To
93 examine whether IL-10 signalling affects immune responses in PV zones, we treated mice with
94 an anti-IL-10R blocking antibody and performed intravital imaging to observe neutrophil
95 behaviours upon the laser-induced tissue damages. Neutrophil accumulation at damage sites in

PV zones was significantly increased by IL-10 signalling blockade (**Fig. 2c, Supplementary Video 4**), indicating that IL-10 from MP2 is crucial for limiting inflammatory responses in PV zones. To investigate the molecular mechanism by which IL-10 regulates neutrophil behaviours, we investigated its effects on the liver-resident cells, particularly in liver sinusoidal endothelial cells (LSECs) and Kupffer cells. We first investigated the spatial expression of the adhesion molecule ICAM-1, the ligand of $\alpha_{M.}$ integrin (Mac1 or CD11b), which has reportedly been crucial for neutrophil adhesion to the liver[17]. We classified LSECs based on CD117 expression: CD117-positive and CD117-negative indicate peri-central venous and peri-portal LSECs, respectively[6], and revealed that ICAM-1 expression was significantly higher in $CD117^+$ LSECs than that in $CD117^-$ LSECs (**Extended Data Fig. 5a-c**). Next, we examined whether administering anti-IL-10R antibodies could increase ICAM-1 expression on the periportal $CD117^-$ LSECs, and found that ICAM-1 expression increased in peri-portal LSECs (**Extended Data Fig. 5d**). These results suggest that IL-10 locally produced by MP2 suppresses ICAM-1 expression on LSECs, thereby inhibiting neutrophil adhesion to the PV zones. Furthermore, we found that blockade of IL-10 signalling elevated the expression level of chemokines, *Cxcl1* and *Cxcl2* in Kupffer cells and periportal LSECs, respectively (**Extended Data Fig. 5e**). These chemokines activate the "inside-out" signalling of integrins in neutrophils, which rapidly changes the integrin structure from the bent form to the upright form, and enhances its binding affinity to the ligands[18]. We also confirmed an increase in staining intensity of $\alpha_{M.}$ integrin on

115 neutrophil using fluorescein isothiocyanate (FITC)-conjugated antibodies when blocking IL-
116 10 signalling (**Extended Data Fig. 5f, g**). Additionally, we observed that blockade of IL-10R
117 increased the number of resident Kupffer cells expressing TIM-4, which is known as a marker
118 for endogenous Kupffer cells differentiated from embryonic stem cell progenitors[19], but their
119 polarised distribution was retained (**Supplementary Fig. 4**). The increased density of Kupffer
120 cells with elevated chemokine expressions may synergistically promote neutrophil adhesion to
121 LSECs. Therefore, IL-10 locally secreted from MP2 may act on LSECs and Kupffer cells in
122 periportal regions, suppressing neutrophil adhesion in the two distinct manners. However,
123 administering anti-IL-10R antibodies itself did not affect the number of infiltrating neutrophils
124 in the liver (**Extended Data Fig. 5h**).

125 Flow cytometrical analysis detected a positive correlation between Marco expression and
126 *Il10* transcriptional activity in Kupffer cells (**Extended Data Fig. 4b**), suggesting the
127 functional role of Marco for immunosuppressive (IL-10 producing) activity. Next, we
128 evaluated *Il10* mRNA expression in wild-type ($Marco^{+/+}$) and *Marco* knockout ($Marco^{-/-}$)
129 Kupffer cells and found that *Il10* expression was significantly decreased under *Marco*-deficient
130 conditions (**Extended Data Fig. 4c**). This result suggests that signalling downstream of Marco
131 stimulates the production of anti-inflammatory cytokines, such as IL-10. Intravital imaging
132 using the laser-induced damage model also verified that *Marco* knockout animals exhibited
133 enhanced inflammatory responses to the damages in PV zones due to the lack of IL-10 signals

(**Fig. 2d, Extended Data Fig. 4c, Supplementary Video 5**), suggesting a critical function for the Marco-IL-10 axis for exerting the anti-inflammatory effects of MP2.

Marco is known as a scavenger receptor for damage-associated molecular patterns (DAMPs) and a broad range of polyanionic substances released from bacteria[20–22]. Since the expression level of Marco in MP2 is significantly higher than those of other pattern recognition receptors, such as TLR2 and TLR4, in periportally residing cells (**Supplementary Fig. 5**), we hypothesised that Marco may also directly contribute to the immunosuppressive phenotype in PV zones by sequestrating these immunostimulatory factors[20,23,24]. To address this issue, we visualised the pathogen-capturing activity of $Marco^+$ and $Marco^-$ Kupffer cells in vitro and in vivo, and demonstrated that $Marco^+$ Kupffer cells preferentially captured fluorescently labelled bacteria (**Extended Data Fig. 6**), suggesting that $Marco^+$ MP2 Kupffer cells exert an anti-inflammatory effect via Marco-dependent sequestration of immunogenic pathogens, in addition to producing abundant anti-inflammatory cytokines, such as IL-10.

The liver is directly connected to the gut via the portal vein. Gut commensal microbes or their components, such as lipopolysaccharide (LPS) or metabolites, can easily flow into the liver through the portal vein[25]. Next, we examined the effect of gut commensals on the generation and function of MP2 Kupffer cells. We quantified the MP2 subset in specific pathogen-free (SPF), germ-free (GF), and antibiotic-treated (ABX) mice. To analyse the contribution of pathogen-associated molecular patterns (PAMPs), we compared the findings

153 with those from MyD88 knockout mice (MyD88$^{-/-}$) lacking a critical downstream adaptor
154 protein of PAMP receptors. The absolute numbers of sinusoidal F4/80^{+} macrophages (Kupffer
155 cells) were almost the same under all conditions, irrespective of their location within a lobule.
156 However, the percentages of Marco^{+} MP2 in GF, ABX, and MyD88$^{-/-}$ mice were significantly
157 decreased compared to those in SPF controls (**Fig. 3a, b, c**). With a decrease in MP2, both
158 Kupffer cells and tissue lysates exhibited reduced *Il10* expression under gut commensal
159 bacteria-depleted conditions compared to SPF controls (**Fig. 3d, e)**. To examine whether the
160 decrease in MP2 by depleting gut commensal microbes affects inflammatory responses in PV
161 zones, we performed intravital imaging using antibiotic-treated mice to detect local
162 inflammatory responses upon the laser-induced damages. Neutrophil accumulation in PV zones
163 was significantly enhanced by gut commensal depletion (**Fig. 3f, Supplementary Video 6**),
164 suggesting the critical role of commensal microbe-induced MP2 in the immunosuppressive
165 activity within PV zones.

166 Coincidentally, we found that MP2 numbers varied between mice under different housing
167 conditions (SPF-A and SPF-B mice). A larger population of MP2 was observed in SPF-A (**Fig.**
168 **4a**). We then performed 16S ribosomal RNA (rRNA)-sequencing analysis using the colorectal
169 contents and identified five bacterial candidates that might induce MP2 (**Extended Data Fig.**
170 **7a-c**). Based on the positive correlation between the relative abundance of bacteria and the
171 percentage of Marco^{+} MP2, we focused on a bacterial family, Odoribacteraceae, which belongs

172 to the order Bacteroidales and has recently been shown to be involved in the longevity of
173 “centenarians”[26] **(Fig. 4b, c)**. To determine whether Odoribacteraceae contributes to MP2
174 induction, we inoculated an Odoribacteraceae strain (Odori) or a *Bacteroides stercoris* strain
175 (Stercoris) as the negative control into germ-free mice. In parallel, we transplanted Odori or
176 Stercoris into antibiotic-treated mice and kept the mice with SPF mice in the same cage.
177 Although neither Stercoris nor Odori alone significantly induced MP2 (**Fig. 4d**), MP2
178 induction was augmented under symbiosis of Odori and other commensals (**Fig. 4e**). These
179 results indicated that Odoribacteraceae is critical but not sufficient for inducing MP2.
180 Odoribacteraceae is reportedly associated with bile acid metabolism in the gut lumen and
181 contributes to the production of isoallo-lithocholic acid (isoallo-LCA) from chenodeoxycholic
182 acid-derived metabolites, such as 3-oxoallo-LCA and Δ4-isoLCA, which are supplied by other
183 commensals[26,27]. We measured isoallo-LCA contents in the faeces under the conditions of GF,
184 gnotobiote with Odori alone, and SPF with/without Odori and confirmed that concentration of
185 isoallo-LCA was more than 10-fold higher in the SPF condition with Odori compared with that
186 in other conditions (**Fig. 4f**). This suggests that the symbiosis of Odori and other bacteria is
187 necessary for a sufficient supply of isoallo-LCA. Finally, we examined whether oral
188 administration of isoallo-LCA enhanced MP2 induction and revealed that isoallo-LCA
189 significantly stimulates the induction of $Marco^{+}$ Kupffer cells and increases the expression
190 levels of *Il10* mRNA (**Fig. 4g, h**), suggesting that the effect of Odoribacteraceae on MP2

191 induction is partly mediated by the postbiotic activity such as producing isoallo-LCA.

192 Regarding the physiological significance of the preferential distribution of MP2 in PV
193 zones, a plausible hypothesis is that specific amounts of gut commensals or their related
194 DAMPs/PAMPs can constitutively reach the liver via the portal vein[25], and MP2 may protect
195 against unfavourable inflammatory responses to such pathogens, especially at the entrance of
196 the liver, that is, hepatic periportal regions. This immunomodulatory mechanism would become
197 critical when the intestinal barrier is impaired, causing an increased number of pathogens to be
198 translocated into the liver, as observed in patients with colitis[28], non-alcoholic fatty liver
199 disease[29,30], autoimmune hepatitis[31,32], obesity[33], and diabetes[33]. To verify this hypothesis, we
200 generated a dextran sodium sulphate (DSS)-induced acute colitis model using *Marco*$^{+/+}$ (wild-
201 type) and *Marco*$^{-/-}$ (knockout) mice and analysed inflammatory responses in the liver. In this
202 model, 1% DSS was orally administered for 1 week, and the livers were analysed after an
203 additional 4 days of normal water feeding (**Extended Data Fig. 8a**). In the results, Kupffer
204 cells from *Marco*$^{-/-}$ mice exhibited decreased production of anti-inflammatory cytokines
205 compared with those from wild-type controls (**Extended Data Fig. 8b**), and consistently,
206 intravital imaging revealed substantially higher infiltration of inflammatory neutrophils into
207 the liver in *Marco*$^{-/-}$ mice on day 11 (**Extended Data Fig. 8c, d, Supplementary Video 7**). In
208 accordance with the occurrence of the inflammation, *Marco*$^{-/-}$ mice exhibited a significant
209 reduction in body weight (**Extended Data Fig. 8e**). Next, we introduced a mouse model of

chronic colitis by repetitive challenges with DSS to analyse the effect of chronic gut inflammation on the liver (**Fig. 5a**), representing a significant increase in inflammatory lymphocytes (T helper 17 cell: Th17) and neutrophils in the liver of *Marco*$^{-/-}$ mice compared to those in wild-type controls (**Fig. 5b, c**). Intravital imaging indicated an accumulation of inflammatory neutrophils near the portal veins in *Marco*$^{-/-}$ mice (**Fig. 5d, Supplementary Video 8**). Consistently, serum markers for hepatic damage, including alanine aminotransferase (ALT) and aspartate aminotransferase (AST), were elevated in *Marco*$^{-/-}$ mice (**Fig. 5e**). Furthermore, the expression levels of the fibrosis markers, *Timp1* and *Col1a1*[32], were also increased, leading to type I collagen accumulation in periportal areas in *Marco*$^{-/-}$ mice (**Fig. 5f, g**). Such phenotypes in the *Marco*-deficient condition resemble those observed in chronic human inflammatory liver diseases, such as primary sclerosing cholangitis (PSC). Primary sclerosing cholangitis, an intractable disease of unknown origin that is characterised by chronic inflammation around the bile duct and portal vein regions, leads to progressive fibrosis and sclerosis in these areas[34,35]. Notably, PSC is often complicated by inflammatory bowel diseases and has been associated with microbial translocation from the inflamed gut[34,36,37]. Using clinical liver samples of patients with PSC as well as control liver specimens (six PSC and nine normal control samples), we performed immunofluorescence staining to detect Marco^{+} and Marco^{-} macrophages, demonstrating that the number of periportal Marco^{+} macrophages, corresponding to MP2 in the murine liver, was significantly decreased in the PSC livers

compared to those in the controls. However, the number of total macrophages was comparable between PSC and control liver specimens (**Fig. 5h, i**). These results may suggest that Marco-expressing macrophages are present in the human liver, which could be associated with chronic inflammatory liver diseases, such as PSC.

Next, we examined the possible roles of MP2 Kupffer cells in non-alcoholic fatty liver disease (NAFLD)/non-alcoholic steatohepatitis (NASH), a common and intractable chronic inflammatory disorder in the liver, often complicated with the leaky gut syndrome[29,30]. Based on the reanalysis of the single-cell data from patients with cirrhosis, the MP2 population was reduced in patients with NAFLD compared with the normal controls (**Extended Data Fig. 3g**), implying that MP2 might be involved in the disease progress. To reveal the relationship between MP2 abundance and NAFLD/NASH development, we used a murine NASH/NAFLD model by feeding a methionine-/choline-deficient high-fat (MCDHF) diet to mice for up to 6 weeks and harvested the livers in 2-week increments (**Extended Data Fig. 9a**). As a result, the resident Marco^{+} TIM-4^{+} MP2 population was significantly declined by 64.5 % in the first 2 weeks (**Extended Data Fig. 9b, c**), which was inversely correlated to the occurrence of inflammatory symptoms, such as elevation of serum AST/ALT and neutrophil infiltration (**Extended Data Fig. 9d-i**). The correlation coefficients between MP2 presence and these symptoms were $R = -0.82$ for AST, $R = -0.76$ for ALT, and $R = -0.59$ for neutrophil accumulation, indicating strong negative correlations (**Extended Data Fig. 9e, g, i**). These

results suggest that the severity of the disease activity depends on the paucity level of MP2. We then fed MCDHF diet to *Marco*$^{-/-}$ (knockout) mice lacking the anti-inflammatory functions of MP2 and detected a more severe liver inflammation (**Extended Data Fig. 9j**) and deteriorated liver histopathology representing a more severe steatosis around the portal veins (**Extended Data Fig. 9k. l**). The low value of AST/ALT ratio in *Marco*$^{-/-}$ mice implies the stress-induced damages in PV zones or more advanced fatty liver disease in *Marco*$^{-/-}$ mice (**Extended Data Fig. 9m**). We also verified that Marco^{+} MP2 was significantly decreased in human NAFLD/NASH patients (seven samples) compared to the normal controls (nine samples) (**Extended Data Fig. 9n-p**). The pathohistological samples can be classified based on the severity of NAFLD/NASH groups according to the 'Matteoni scoring system'[38], and we could demonstrate that the number of MP2 was remarkably decreased in NASH (more severe) group, compared to those in NAFLD (less severe) group (**Extended Data Fig. 9p**). These results may suggest that Marco-expressing macrophages could be associated with the progression of chronic inflammatory liver diseases, such as NAFLD/NASH as well as PSC.

The spatial heterogeneity of constituent cells is critical for tissue integrity. By combining in vivo spatiotemporal imaging and single-cell transcriptomic analyses, we demonstrated the heterogenous immune responsiveness in specific liver segments and newly identified an immunosuppressive Marco-expressing resident macrophage (Kupffer cell) subset, designated as MP2, which preferentially localises in PV zones. The presence of PV-polarised Marco^{+}

267 immunosuppressive Kupffer cells are further supported by previous studies showing higher
268 phagocytic function of periportal Kupffer cells[39] and IL-10 production in response to PAMPs
269 stimulation[40]. Scavenging exogenous toxins, including bacteria, PAMPs, and DAMPs, have
270 been demonstrated to serve as a firewall in the body[41,42]; the concept is well consistent with the
271 function of Marco demonstrated in this study. In 2021, Bleriot *et al*. and Simone *et al*. proposed
272 subsets of Kupffer cell, KC1 and KC2[43,44]. KC2 was regarded as a minor population expressing
273 CD206 and ESAM as markers for this specific population and involved in regulating oxidative
274 stress under fatty liver conditions[43] and activation of $CD8^+$ cytotoxic T cells during hepatitis B
275 virus infection[44]. Nevertheless, regarding the KC2, an immunosuppressive phenotype or
276 polarised distribution towards PV zones has not been reported, and we concluded that
277 KC1/KC2 is a conceptually different classification from MP1/MP2 in this study. Nevertheless,
278 based on the cell markers, we also checked that the $Marco^+$ MP2 subset does not belong to
279 KC2 but instead belongs to KC1 (**Extended Data Fig. 10a-c**). Therefore, MP2 can be redefined
280 as a subset of KC1 and be referred to as "$Marco^+$ KC1" (**Extended Data Fig. 10d**).

281 Developmental origin provides an important clue for understanding macrophage
282 characteristics. Macrophages in the adult body are supplied via two pathways: primitive
283 macrophages are obtained from erythro-myeloid progenitors (EMPs) in the yolk sac, and
284 during later development, additional macrophages are supplied by hematopoietic stem cells in
285 the bone marrow[45,46]. Macrophages from different origins exhibit different cellular properties

and functions. For example, yolk sac-derived macrophages have higher self-renewal[45,46] and immunoregulatory[47,48] properties than bone marrow-derived macrophages. To examine the origin of MP1 and MP2 in the liver, we performed parabiosis experiments using CX_3CR1-tdTomato and wild-type parabionts and revealed that both MP1 and MP2 were hardly replaced by the bone marrow-derived circulating populations for up to 20 weeks. Looking into the small number of replaced tdTomato$^+$ macrophages in wild-type parabionts, more than 90 % of these were Marco-negative (**Extended Data Fig. 11a-c**). Also, the bone marrow-derived macrophages did not express TIM-4, a yolk sac-derived resident macrophage marker[19](**Extended Data Fig. 11d**). These results suggest that MP2 is essentially derived from EMPs with high self-renewing capacity and rarely differentiated from hematopoietic stem cells in the bone marrow during the postnatal development. We next deleted the liver resident macrophages with CLL to verify this perspective and analysed the regenerated Kupffer cells after 6 weeks (**Extended Data Fig. 11e-j**). We classified the macrophages using the resident macrophage marker TIM-4 and found that the CLL-treated liver contained survived resident (TIM-4-positive) and bone marrow-derived (TIM-4-negative) populations (**Extended Data Fig. 11f-h**). TIM-4$^+$ resident macrophages showed greater percentage of Marco-expressing cells and higher expression of *Il10* mRNA compared to TIM-4$^-$ bone marrow-derived macrophages (**Extended Data Fig. 11i, j**). Beattie *et al.* also compared yolk sac-derived Kupffer cells with bone marrow-derived ones by ingeniously creating the chimeric mice. They

305 demonstrated that the bone marrow-derived Kupffer cells did not express Marco, even when
306 stimulated by LPS[49]. The bulk of these results suggests that MP2 should be supplied from
307 EMPs in the yolk sac. Nevertheless, detailed analyses using fate-mapping system are required
308 to elucidate when and how MP1 and MP2 are generated during the liver development.

309 Commensal bacteria and their related pathogens/metabolites that translocate from the gut
310 to the liver contribute to MP2 development in PV zones, which, in turn, suppresses excessive
311 inflammation at the gateway of bacterial entry and maintains homeostasis in the liver. The
312 mechanisms underlying commensal bacteria-induced generation of MP2 remain to be
313 elucidated. However, pattern recognition receptor stimulation by PAMPs or DAMPs in some
314 subpopulations of liver-resident cells, including macrophages (Kupffer cells) and endothelial
315 cells, appears to be involved. In this study, we demonstrated that a specific family of
316 commensals, Odoribacteraceae, enhanced MP2 induction by supplying a characteristic bile
317 acid metabolite, isoallo-LCA. Isoallo-LCA induces structural changes in the chromatin and
318 facilitates DNA binding of transcription factors, particularly the nuclear hormone receptor
319 NR4A1[27]. In macrophages, NR4A1 plays a critical role in inducing anti-inflammatory
320 properties, such as elevating IL-10 production[50]. Because Kupffer cells also express abundant
321 NR4A1, this molecule may be involved in MP2 differentiation. Additionally, under depleting
322 the gut commensals with antibiotic treatment, oral administration of isoallo-LCA did not induce
323 MP2 (**Extended Data Fig. 7d-f**), suggesting that the interaction of Odoribacteraceae and other

bacteria is necessary not only for a sufficient production of isoallo-LCA but also for the induction of MP2 by isoallo-LCA. This is consistent with the present results that Odoribacteraceae could enhance the generation of MP2 when co-existence with other commensals under SPF conditions but could not solely induce MP2 (**Fig. 4d, e**).

This study demonstrated the biological significances of the spatially heterogeneous distribution of Kupffer cell subsets with distinct functions. As a gateway from the gut, the liver is inherently vulnerable to external pathogens, and PV zones are prone to inflammation due to biased accumulation of immune cells, especially Kupffer cells[6,9]. The present results led to a novel concept that the immunomodulatory activity of MP2 in liver PV zones is critical for maintaining healthy conditions against gut commensal infection, and disruption of this protective mechanism may be correlated with intractable liver diseases, such as PSC and NASH. Also, our comprehensive analyses with laboratory animals and human samples demonstrated that MP2 could be a promising target for developing therapeutic approaches against these refractory liver diseases.

Main references

1. Jungermann, K. & Kietzmann, T. Zonation of parenchymal and nonparenchymal metabolism in liver. *Annu. Rev. Nutr.* **16**, 179–203 (1996).

2. Mizukami, K. *et al.* In vivo O_2 imaging in hepatic tissues by phosphorescence lifetime imaging microscopy using Ir(III) complexes as intracellular probes. *Sci. Rep.* **10**, 1–14 (2020).

3. Nauck, M., Wölfle, D., Katz, N. & Jungermann, K. Modulation of the glucagon-dependent induction of phosphoenolpyruvate carboxykinase and tyrosine aminotransferase by arterial and venous oxygen concentrations in hepatocyte cultures. *Eur. J. Biochem.* **119**, 657–661 (1981).

4. Jungermann, K., Heilbronn, R., Katz, N. & Sasse, D. The glucose/glucose-6-phosphate cycle in the periportal and perivenous zone of rat liver. *Eur. J. Biochem.* **123**, 429–436 (1982).

5. Jungermann, K. & Katz, N. Functional specialization of different hepatocyte populations. *Physiol. Rev.* **69**, 708–764 (1989).

6. Gola, A. *et al.* Commensal-driven immune zonation of the liver promotes host defence. *Nature* **589**, 131–136 (2021).

7. Su, T. *et al.* Single-cell transcriptomics reveals zone-specific alterations of liver sinusoidal endothelial cells in cirrhosis. *Cmgh* **11**, 1139–1161 (2021).

8. Dobie, R. *et al.* Single-cell transcriptomics uncovers zonation of function in the mesenchyme during liver fibrosis. *Cell Rep.* **29**, 1832-1847 (2019).

9. Guilliams, M. *et al.* Spatial proteogenomics reveals distinct and evolutionarily conserved hepatic macrophage niches. *Cell* **185**, 379-396 (2022).

10. Halpern, K. B. *et al.* Single-cell spatial reconstruction reveals global division of labour in the mammalian liver. *Nature* **542**, 352–356 (2017).

11. Dal-Secco, D. *et al.* A dynamic spectrum of monocytes arising from the in situ reprogramming of CCR2^{+} monocytes at a site of sterile injury. *J. Exp. Med.* **212**, 447–456 (2015).

12. Remmerie, A. *et al.* Osteopontin expression identifies a subset of recruited macrophages distinct from Kupffer cells in the fatty liver. *Immunity* **53**, 641-657 (2020).

13. Scott, C. L. *et al.* Bone marrow-derived monocytes give rise to self-renewing and fully differentiated Kupffer cells. *Nat. Commun.* **7**, 1–10 (2016).

14. English, K. *et al.* The liver contains distinct interconnected networks of CX3CR1^{+} macrophages, XCR1^{+} type 1 and CD301a^{+} type 2 conventional dendritic cells embedded within portal tracts. *Immunol. Cell Biol.* **100**, 394–408 (2022).

15. Ramachandran, P. *et al.* Resolving the fibrotic niche of human liver cirrhosis at single-cell level. *Nature* **575**, 512-518 (2019).

16. MacParland, S. A. *et al.* Single cell RNA sequencing of human liver reveals distinct

intrahepatic macrophage populations. *Nat. Commun.* **9**, 1–21 (2018).

17. McDonald, B. *et al.* Intravascular danger signals guide neutrophils to sites of sterile inflammation. *Science* **330**, 362–6 (2010).

18. Lefort, C. T. & Ley, K. Neutrophil arrest by LFA-1 activation. *Front. Immunol.* **3**, 1–10 (2012).

19. Sakai, M. *et al.* Liver-derived signals sequentially reprogram myeloid enhancers to initiate and maintain Kupffer cell identity. *Immunity* **51**, 655-670 (2019).

20. Shichita, T. *et al.* MAFB prevents excess inflammation after ischemic stroke by accelerating clearance of damage signals through MSR1. *Nat. Med.* **23**, 723–732 (2017).

21. Andersson, L. & Freeman, M. W. Functional changes in scavenger receptor binding conformation are induced by charge mutants spanning the entire collagen domain. *J. Biol. Chem.* **273**, 19592–19601 (1998).

22. Ojala, J. R. M., Pikkarainen, T., Tuuttila, A., Sandalova, T. & Tryggvason, K. Crystal structure of the cysteine-rich domain of scavenger receptor MARCO reveals the presence of a basic and an acidic cluster that both contribute to ligand recognition. *J. Biol. Chem.* **282**, 16654–16666 (2007).

23. Mukhopadhyay, S. *et al.* SR-A/MARCO-mediated ligand delivery enhances intracellular TLR and NLR function, but ligand scavenging from cell surface limits TLR4 response to pathogens. *Blood* **117**, 1319–1328 (2011).

24. Jing, J. *et al.* Role of macrophage receptor with collagenous structure in innate immune tolerance. *J. Immunol.* **190**, 6360–6367 (2013).

25. Leinwand, J. C. *et al.* Intrahepatic microbes govern liver immunity by programming NKT cells. *J. Clin. Invest.* **132**, e151725 (2022).

26. Sato, Y. *et al.* Novel bile acid biosynthetic pathways are enriched in the microbiome of centenarians. *Nature* **599**, 458–464 (2021).

27. Li, W. *et al.* A bacterial bile acid metabolite modulates Treg activity through the nuclear hormone receptor NR4A1. *Cell Host Microbe* **29**, 1366-1377 (2021).

28. Spadoni, I. *et al.* A gut-vascular barrier controls the systemic dissemination of bacteria. *Science* **350**, 830–834 (2015).

29. Sookoian, S. *et al.* Intrahepatic bacterial metataxonomic signature in non-alcoholic fatty liver disease. *Gut* **69**, 1483–1491 (2020).

30. Luther, J. *et al.* Hepatic injury in nonalcoholic steatohepatitis contributes to altered intestinal permeability. *Cell. Mol. Gastroenterol. Hepatol.* **1**, 222–232 (2015).

31. Manfredo Vieira, S. *et al.* Translocation of a gut pathobiont drives autoimmunity in mice and humans. *Science* **360**, 1156–1161 (2018).

32. Nakamoto, N. *et al.* Gut pathobionts underlie intestinal barrier dysfunction and liver T helper 17 cell immune response in primary sclerosing cholangitis. *Nat. Microbiol.* **4**, 492–503 (2019).

414 33. Thaiss, C. A. *et al.* Hyperglycemia drives intestinal barrier dysfunction and risk for
415 enteric infection. *Science* **359**, 1376–1383 (2018).
416 34. Lazaridis, K. N. & LaRusso, N. F. Primary sclerosing cholangitis. *N. Engl. J. Med.* **375**,
417 1161–1170 (2016).
418 35. Dyson, J. K., Beuers, U., Jones, D. E. J., Lohse, A. W. & Hudson, M. Primary sclerosing
419 cholangitis. *Lancet* **391**, 2547–2559 (2018).
420 36. Horsley-Silva, J. L., Carey, E. J. & Lindor, K. D. Advances in primary sclerosing
421 cholangitis. *Lancet Gastroenterol. Hepatol.* **1**, 68–77 (2016).
422 37. O'Toole, A. *et al.* Primary sclerosing cholangitis and disease distribution in
423 inflammatory bowel disease. *Clin. Gastroenterol. Hepatol.* **10**, 439–441 (2012).
424 38. Matteoni, C. A. *et al.* Nonalcoholic fatty liver disease: A spectrum of clinical and
425 pathological severity. *Gastroenterology* **116**, 1413–1419 (1999).
426 39. Bouwens, L., Baekeland, M., De Zanger, R. & Wisse, E. Quantitation, tissue distribution
427 and proliferation kinetics of Kupffer cells in normal rat liver. *Hepatology* **6**, 718–22
428 (1986).
429 40. Knoll, P. *et al.* Human Kupffer cells secrete IL-10 in response to lipopolysaccharide
430 (LPS) challenge. *J. Hepatol.* **22**, 226–229 (1995).
431 41. Balmer, M. L. *et al.* The liver may act as a firewall mediating mutualism between the
432 host and its gut commensal microbiota. *Sci. Transl. Med.* **6**, 237ra66 (2014).

42. van der Laan, L. J. *et al.* Regulation and functional involvement of macrophage scavenger receptor MARCO in clearance of bacteria in vivo. *J. Immunol.* **162**, 939–47 (1999).

43. Blériot, C. *et al.* A subset of Kupffer cells regulates metabolism through the expression of CD36. *Immunity* **54**, 2101-2116 (2021).

44. De Simone, G. *et al.* Identification of a Kupffer cell subset capable of reverting the T cell dysfunction induced by hepatocellular priming. *Immunity* **54**, 2089-2100 (2021).

45. Yona, S. *et al.* Fate mapping reveals origins and dynamics of monocytes and tissue macrophages under homeostasis. *Immunity* **38**, 1073–1079 (2013).

46. Liu, Z. *et al.* Fate mapping via Ms4a3-expression history traces monocyte-derived cells. *Cell* **178**, 1509-1525 (2019).

47. van de Laar, L. *et al.* Yolk sac macrophages, fetal liver, and adult monocytes can colonize an empty niche and develop into functional tissue-resident macrophages. *Immunity* **44**, 755–768 (2016).

48. Tran, S. *et al.* Impaired Kupffer cell self-renewal alters the liver response to lipid overload during non-alcoholic steatohepatitis. *Immunity* **53**, 627-640 (2020).

49. Beattie, L. *et al.* Bone marrow-derived and resident liver macrophages display unique transcriptomic signatures but similar biological functions. *J. Hepatol.* **65**, 758–768 (2016).

50. Koenis, D. S. *et al.* Nuclear Receptor Nur77 Limits the Macrophage Inflammatory Response through Transcriptional Reprogramming of Mitochondrial Metabolism. *Cell Rep.* **24**, 2127-2140 (2018).

Figure Legends

Fig. 1. A periportal macrophage subset suppressively regulates periportal immune activation. a, Spatial transcriptomics showing hepatic zonation (n = 4): gene expression of *Cyp2f2* (left-upper) and *Cyp2e1* (left-lower), identified zones (right-upper, blue: PV zones, orange: CV zones, green: marginal zones), and H&E staining (right-lower). **b**, Immune pathways enriched in PV zones (vs. CV zones). P-values were determined using one-sided Fisher's exact test. **c**, Representative intravital images of in situ inflammatory responses of neutrophils against sterile laser-induced damages in control (top) and macrophage-depleted mice (bottom) [n = 14 each, green: neutrophils, white: damaged sites (autofluorescence), and blue: collagens visualised using second harmonic generation (SHG)]. Scale bar: 100 μm. **d**, Neutrophil accumulation scores in control (left) and macrophage-depleted mice (right). Data are presented as means ± standard error of the mean (SEM). P-value was determined using paired two-sided Mann–Whitney U test at 3 h. **e**, Schematics of isolation of zone-specifically labelled immune cells. Scale bar: 50 μm. **f**, t-Distributed Stochastic Neighbour Embedding (tSNE) plot depicting each immune cell cluster and location (left). The localisation score (PV/CV ratio) (right). **g**, Expression of *Clec4f* and *Marco* shown on the tSNE plot. **h**, Violin plots depicting expression of the anti-inflammatory cytokines *Il10*, *Il1rn*, *and Tgfb1* in MP1 and MP2. Statistical significance was determined using a two-sided Wilcoxon Rank Sum test.

i, Representative immunofluorescence image showing Marco (green), F4/80 (red), and E-cadherin (blue) (left, n = 4, 33 visual fields). Localisation score (PV/CV ratio) of $Marco^+$ and $Marco^-$ macrophages (right). Scale bar: 100 µm. Data are presented as means (asterisk) with medians, smallest observations, lower and upper quartiles, and largest observations. Statistical significance was determined using unpaired two-sided Mann–Whitney U test. The exact *p*-value is 2.2×10^{-16}.

Fig. 2. The Marco–IL-10 axis is necessary for establishing an immunosuppressive niche in periportal regions. a, mRNA expression of *Il10* in MP2 and other immune cell types identified in the single-cell transcriptomics. Statistical significance was determined using a two-sided Wilcoxon Rank Sum test. The *p*-value was adjusted based on Bonferroni correction. **b**, Relative mRNA expression of *Il10* to *Gapdh* in MP2 (n = 6), LSECs (n = 8), HSCs (n = 7), and hepatocytes (n = 6). **c**, Representative intravital images of in situ inflammatory responses of neutrophils upon laser-induced tissue damages under treatment with isotype control antibody (left) and anti-IL-10R antibody (centre) [n = 6 per condition, green: neutrophils, white: damaged sites (autofluorescence), and blue: SHG (tissue collagens)]. Scale bar: 100 μm. Spatially biased neutrophil accumulation at 3 h post-laser ablation is shown as the PV/CV ratio (right). **d**, Representative intravital images of in situ inflammatory responses of neutrophils upon laser-induced tissue damages in *Marco*$^{+/+}$ wild-type (left, n = 10) and *Marco*$^{-/-}$ knockout (centre, n = 7) mice [green: neutrophils, white: damaged sites, and blue: SHG (tissue collagens)]. Scale bar: 100 μm. Spatially biased neutrophil accumulation at 3 h post-laser ablation is shown as the PV/CV ratio (right). All quantitative data are presented as means (asterisk) with medians, smallest observations, lower and upper quartiles, and largest observations. Statistical significance was determined using unpaired two-sided Mann–Whitney U test.

Fig. 3. Gut commensal microbes induce the periportal immunosuppressive Kupffer cells. **a**, Representative immunofluorescence images showing Marco (green), F4/80 (red), and E-cadherin (blue) in liver sections from specific pathogen-free (SPF, n = 11, 35 visual fields), germ-free (GF, n = 5, 27 visual fields), antibiotic-treated (ABX, n = 9, 26 visual fields), and MyD88 knockout mice (*MyD88*$^{-/-}$, n = 5, 39 visual fields). Scale bar: 100 μm. **b**, Absolute number of F4/80-positive cells (total Kupffer cells) per visual field. **c**, Percentage of Marco^{+} immunosuppressive Kupffer cells (MP2) to total Kupffer cells quantified using flow cytometry. **d**,**e**, Relative mRNA expression of *Il10* to *Gapdh* in total Kupffer cell fractions (d) and tissue lysates (e) from SPF control (n = 9) and ABX (n = 7) mice. **f**, Representative intravital images of in situ inflammatory responses of neutrophils upon laser-induced damage in control (left, n = 10) and ABX (centre, n = 12) mice [green: neutrophils, white: damaged sites, and blue: SHG (tissue collagens)]. Scale bar: 100 μm. Spatially biased neutrophil accumulation at 3 h post-laser ablation is shown as the PV/CV ratio (right). All quantitative data are presented as means (asterisk) with medians, smallest observations, lower and upper quartiles, and largest observations. Statistical significance was determined using unpaired two-sided Mann–Whitney U test.

Fig. 4. Odoribacteraceae promotes induction of the periportal immunosuppressive Kupffer cells by providing isoallo-lithocholic acids. **a**, Percentage of Marco^{+} immunosuppressive Kupffer cells (MP2) to total Kupffer cells from SPF-A and SPF-B mice. **b**, Relative abundance (%) of Odoribacteraceae in colorectal contents from SPF-A and SPF-B mice. **c**, Correlation between the abundance of Odoribacteraceae and the percentage of MP2. 'R' indicates the correlation coefficient. **d**, Graphical protocol for generating gnotobiotic mice (left). Odori and Stercoris indicate Odoribacteraceae and *B. Stercoris*, respectively. Percentage of MP2 to total Kupffer cells (right). **e**, Graphical protocol for generating symbiotic conditions of target and SPF microbes (left). Sterile PBS-inoculated GF mice were used as a negative control. Percentage of MP2 to total Kupffer cells (right). **f**, Concentration of isoallo-lithocholic acid (isoallo-LCA) in faeces. **g**, Graphical protocol for oral administration of isoallo-LCA or the vehicle control, dimethyl sulfoxide (DMSO) (left). Percentage of MP2 to total Kupffer cells (right). **h**, Fold changes of *Il10* mRNA expression in Kupffer cells. Data were standardized to ensure a control group mean value of '1'. All quantitative data are presented as means (asterisk) with medians, smallest observations, lower and upper quartiles, and largest observations. Statistical significance was determined using unpaired two-sided Mann–Whitney U test.

534

535 **Fig. 5. Periportal immunosuppressive Kupffer cells protect against gut bacteria-driven**
536 **inflammation. a**, Experimental design of chronic colitis-induced liver inflammation. **b**, The
537 heatmap representing fold changes of each immune cell type against the healthy control. **c**,
538 Absolute numbers of CD45-positive cells, neutrophils, and Th17 cells from DSS-treated
539 *Marco*$^{+/+}$ (n = 12) and *Marco*$^{-/-}$ (n = 11) mice. **d**, Representative intravital images of infiltrating
540 LysM-GFP^{+} cells, including neutrophils/macrophages, in DSS-treated *Marco*$^{+/+}$ and *Marco*$^{-/-}$
541 mice on day 39 [n = 3 per condition, green: LysM-GFP^{+} cells, blue: SHG (tissue collagens)].
542 Scale bar: 100 μm. PV, portal vein; CV, central vein. **e**, Serum ALT and AST levels from DSS-
543 treated *Marco*$^{+/+}$ (n = 14) and *Marco*$^{-/-}$ (n = 16) mice. **f**, Relative mRNA expression of fibrosis
544 markers *Timp1* (left) and *Col1a1* (right) to *Gapdh* in tissue lysates from DSS-treated *Marco*$^{+/+}$
545 (n = 12) and *Marco*$^{-/-}$ (n = 11) mice. **g**, Representative immunofluorescence images are shown
546 (left). Scale bar: 100 μm. Quantification of type I collagen accumulations in PV zones:
547 *Marco*$^{+/+}$ (n = 6, 12 visual fields) and *Marco*$^{-/-}$ (n = 7, 14 visual fields). **h,** Representative
548 immunofluorescence images showing MARCO (green), CD68 (red), and CK19 (cyan) in
549 human livers: PSC (n = 6, 18 visual fields) and normal controls (n = 9, 27 visual fields). Scale
550 bar: 100 μm. **i**, Quantified information: the absolute numbers of CD68-positive cells
551 (macrophages) per visual field (left). Percentage of Marco^{+} cells to total macrophages in visual
552 fields (centre). The exact *p*-value is 1.166×10^{-12}. Percentage of periportal Marco^{+}

553 macrophages within 200 μm from bile ducts (right). The exact *p*-value is 1.92×10^{-8}. All

554 quantitative data are presented as means (asterisk) with medians, smallest observations, lower

555 quartiles, upper quartiles, and largest observations. Statistical significance was determined

556 using unpaired two-sided Mann–Whitney U test.

Methods

Mice

C57BL/6 wild-type and germ-free mice were purchased from CLEA Japan, Inc. *Myd88*$^{-/-}$[51] mice were purchased from Oriental Bio Service, Inc. Photoactivatable-GFP (PA-GFP)[52] mice were provided by Dr. Michel Nussenzweig (Rockefeller University). Rosa-tdTomato (Ai9)[53] and Cx3cr1-Cre[45] mice were purchased from the Jackson Laboratory. Generation of *Marco*$^{-/-}$[54], *Il10*-Venus[55], LysM-GFP[56], and CX_3CR1-GFP[57] mice has been described previously. This study used 8–20-week-old female or male mice (no sex difference was confirmed). All mice were randomly housed in groups and selected for the experiments. Mice were fed a normal diet (MF diet; Oriental Yeast Co., Ltd.) and maintained at 23 ± 1.5 °C and 45 ± 15% relative humidity under a 12 h/12 h light/dark cycle in specific pathogen-free animal facilities at Osaka University. All animal experiments were approved by the Institutional Animal Experimental Committee of Osaka University.

Parabiosis

Transgenic mice (Rosa-LSL-tdTomato:Cx3cr1-Cre) were surgically connected to wild-type mice as described previously[58]. Briefly, the lateral skin incisions were made from the elbow to the knee in each mouse, and then the forelimbs and hind limbs were tied together using silk sutures. We made approximately 1 cm incisions in the peritoneum of each mouse, and the mice

were attached them using silk sutures. The skin incisions were closed using stainless steel wound clips.

Drug treatment

To deplete Kupffer cells, we used clodronate liposome according to a previous study[59]. Briefly, 500 μg clodronate liposome (#MKV100, Cosmo Bio) in 200 μL phosphate-buffered saline (PBS) was intravenously injected via the tail vein (**Fig.1**, **Extended Data Fig.2**, **Supplementary Fig. 1**) and 650 μg clodronate liposome in 200 μL PBS was injected in the same way (**Extended Data Fig. 11**). The mice were used for further experiments 2 days later (**Fig.1**, **Extended Data Fig.2**, **Supplementary Fig. 1**) and 6 weeks later (**Extended Data Fig. 11**), respectively. To examine the effects of in vivo blockade of IL-10 signalling, we used an anti-IL-10R antibody based on the method of a previous study[60]. Briefly, 200 μg anti-IL-10R antibody (#112710, BioLegend) or rat IgG1,κ antibody (#400432, BioLegend) as isotype control was intraperitoneally injected every 2 days for 5 days, and the mice were used for the experiments on day 5. To assess MP2 induction by isoallo-lithocholic acid (isoallo-LCA) treatment, we administered 200 μg of isoallo-LCA (#29542, Cayman) via oral gavage. Prior to the administration, 10 mg/mL isoallo-LCA in DMSO was prepared as a stock solution and stored at −80 °C before use. From this stock, 1 mg/mL isoallo-LCA solution was prepared by diluting 10 times with PBS, and 200 μL was administered daily for 2 weeks. As a control, 10%

595 (v/v) DMSO in PBS was administered similarly. To deplete the gut commensals, we treated
596 mice with antibiotics, similar to a previous study[61]. Briefly, 8-week-old mice received 1 g/L
597 ampicillin sodium (#19769-64, Nacalai), 0.5 g/L vancomycin hydrochloride (#36137-91,
598 Nacalai), 1 g/L neomycin sulphate (#19767-84, Nacalai), and 1 g/L metronidazole (#23254-64,
599 Nacalai) in their drinking water for 6 weeks (**Fig, 3 and 4**). The antibiotic-containing water
600 was replaced with a fresh one every 4 days. In **Extended Data Fig. 7d-f**, mice received the
601 same antibiotic-containing water for 1 week, following half the concentration of the complete
602 antibiotic-containing water for 2 weeks during the isoallo-LCA treatment.
603
604 **Spatial transcriptome analysis using Visium™**
605 The mice were euthanised via CO_2 overdose. The liver was immediately excised, and each
606 liver lobe was embedded in Tissue-Tek O.C.T. Compound (Sakura) and snap-frozen in
607 isopentane (Sigma) chilled by liquid nitrogen. The frozen tissue blocks were sliced into 10 µm
608 sections and placed within the capture area of a 10× Visium Spatial Gene expression slide (10×
609 Genomics). The 10x Visium cDNA library was prepared according to the manufacturer's
610 instructions. cDNA libraries from four samples were sequenced on a NovaSeq 6000 (Illumina,
611 USA) platform in a 28+120-base paired-end mode.
612 The raw sequenced reads were processed using 10× Genomics CellRanger 1.0.0. The four
613 sample data were merged to account for the batch effect between samples using Scanorama[62]

and Scanpy[63]. The expression levels of the hepatic zonation markers *Cyp2f2* and *Cyp2e1*[10] were used to classify the Visium spots into portal vein (PV) and central vein (CV) zones. Briefly, the expression levels of *Cyp2f2* and *Cyp2e1* exhibited a bimodal distribution, and the distributions were fitted for each gene using a 'two-component mixed Gaussian model' (**Supplementary Fig. 6**). Establishing a threshold at the junction of the high and low expression distributions should provide a suitable criterion for zonal classification. Visium spots with higher expression of *Cyp2f2* and lower expression of *Cyp2e1* compared with the threshold were defined as PV zones. In contrast, spots with higher expression of *Cyp2e1* and lower expression of *Cyp2f2* compared with the threshold were defined as CV zones. Subsequently, we examined the differentially expressed genes (DEGs) in each zone by statistically comparing the gene expression levels between the identified PV and CV zones with 'Rank genes for characterizing groups' function implemented in Scanpy, and extracted 630 and 340 DEGs, which were enriched in PV and CV zones, respectively. Genes showing adjusted *P*-values (Benjamini-Hochberg method) of more than 0.05 were excluded. We then performed the Gene Ontology analysis using the periportally enriched 630 genes with the software DAVID[64] (version 6.8) and extracted the terms (biological pathways), which contain immune-related genes and show $P < 0.05$.

Intravital imaging of the liver and induction of inflammatory immune responses

All surgical procedures in mice were conducted under anaesthesia with isoflurane (#099-06571, Wako). The left lobe of the liver was surgically exposed and gently placed on a cover glass fixed on the imaging stage. The treated mouse was placed in an environmental dark box and warmed to 37°C by an air heater. The internal surface of the liver was observed using an inverted two-photon excitation microscope (A1R-MP, Nikon, Japan) driven by a laser (Chameleon Vision Ti; Sapphire, Coherent) tuned to 870 nm, with a ×20 water immersion objective lens (CFI LWD Lambda S WI, numerical aperture: 0.95, Nikon). Emission wavelengths were detected via bandpass emission filters at 492/SP nm for the second harmonic generation, 525/50 nm for GFP, 575/25 nm for autofluorescence, and 629/56 nm for Qtracker655. This microscopy system was operated using NIS elements software (Nikon). Qtracker655 Vascular Labels (#Q21021MP, Invitrogen) were diluted 20 times in phosphate-buffered saline (PBS) (#14249-95, Nacalai), and 50 μL of the diluted Qtracker655 Vascular Labels was rapidly administered intravenously through a peripheral intravenous line under imaging to detect the PV and CV zones (**Supplementary Video 9**). Image stacks were collected at 3-μm vertical steps up to a depth of 48 μm below the liver surface at an X–Y resolution of 512 × 512 pixels (1.24 μm/pixel). Raw imaging data were processed using NIS elements (Nikon) and ImageJ software[65]. Two-dimensional maximum-intensity projection (MIP) images were generated using NIS elements. Background subtraction, median filtering, and binarization were performed using ImageJ. The accumulation score was measured as the integrated area of

binarized cells within the region of interest. All images and videos are displayed as MIP images.

To activate local immune cells, we induced necrotic tissue damages measuring < 20 μm using infrared laser pulses within PV and CV zones, at 10–20 μm away from each blood vessel and below the liver capsule, based on the methods of previous studies with minor modifications[66,67]. Intravital imaging commenced immediately after the laser ablation and was performed for 3 h at a time resolution of 30 sec to track the neutrophil movements. Additionally, to observe monocyte/macrophage dynamics, we induced the thermal damages in the liver, and then re-introduced the liver lobe into the mouse body and closed the peritoneum and skin incisions using silk sutures. The mouse was allowed free movement for 24 hours. Monocyte/macrophage accumulation at the damage sites was recorded 24 h post laser ablation (**Extended Data Fig. 2b**).

Zone-specific isolation of leukocytes from the liver

To demarcate the PV zones, we intravenously injected 2 μg of phycoerythrin (PE)-conjugated anti-E-cadherin antibody (#147304, BioLegend) in 200 μL PBS into a PA-GFP mouse. After 20 min, the liver was harvested, and fresh tissue sections (250 μm thickness) were cut using a Vibratome (Leica, Germany) in chilled HBSS (#17461-05, Nacalai) containing 25 mM HEPES (#15630080, Gibco) and 2% foetal bovine serum (FBS) (Lot:12B247, Sigma). The sections were placed on glass-bottom dishes (#627860, Greiner) and then covered with absorbent cotton

671 soaked with a cold buffer. The subsequent procedures were performed in the cooled equipment.
672 Photoactivation in PV or CV zones was performed using a single-photon 405 nm violet laser
673 while observing the sections under a two-photon excitation microscope (A1R-MP, Nikon)[52,68].
674 The photoactivated sections were digested in RPMI medium (#61870036, Gibco) containing
675 10 mM HEPES, 0.033 mg/mL Liberase (#5401119001, Roche), 0.05 mg/mL DNase
676 (#LS002139, Worthington), and 0.35 mM $CaCl_2$ (#036-19731, Wako) for 35 min with agitation.
677 The single-cell suspension was filtered through a 100 μm cell strainer, and the undigested
678 material was mashed through a 100 μm cell strainer before centrifugation at 500 × g for 5 min.
679 The supernatant was discarded, and the pellet was resuspended in 100 μL PBS, followed by
680 the addition of 0.2 μL Zombie NIR solution (#423105, BioLegend), and then the samples were
681 incubated for 15 min at room temperature (RT, approximately 25 °C) to stain dead cells. Finally,
682 400 μL autoMACS running buffer (#130-091-221, Miltenyi) was added before fluorescence-
683 activated cell sorting (FACS) staining.
684
685 **Unbiased isolation of leukocytes from the liver**
686 Liver leukocytes were isolated as described previously[15], with slight modifications. Briefly,
687 the livers were minced into smaller pieces using scissors and then digested in RPMI medium
688 containing 0.625 mg/mL collagenase D (#11088858001, Roche), 0.85 mg/mL collagenase V
689 (#C9263, Sigma), 1 mg/mL dispase (#17105041, Gibco), and 30 U/mL DNase (#10104159001,

690 Roche) for 20 min with agitation at 37 °C. All the subsequent procedures were conducted at
691 4 °C. The single-cell suspension was filtered through a 100 μm cell strainer, and undigested
692 pieces were mashed through a 100 μm cell strainer before centrifuging at 500 × g for 5 min.
693 The supernatant was discarded, and the pellet was resuspended in 5 mL RPMI containing 2%
694 FBS. The cell suspension was added on 5 mL 33% Percoll (#17089102, GE) in a 15-mL Falcon
695 tube, and centrifuged at 800 × g for 20 min at 20 °C. Next, the top 5.5 mL was aspirated and
696 discarded, and the remainder was washed in additional PBS and centrifuged at 500 × g for 5
697 min. The resulting supernatant was discarded, and the pellet was resuspended in ACK lysis
698 buffer (#A1049201, Gibco) for 3 min to remove red blood cells. The cell suspensions were
699 then washed in PBS containing 2% FBS, filtered through a 70 μm cell strainer, and centrifuged
700 at 500 × g for 5 min. The pellet was resuspended in autoMACS running buffer before FACS
701 staining.
702
703 **Isolation of hepatocytes, liver sinusoidal endothelial cells (LSECs), and hepatic stellate**
704 **cells (HSCs)**
705 Hepatocytes, LSECs, and HSCs were isolated as described previously[69]. Briefly, the livers
706 were perfused with EGTA (#E3889, Sigma) solution and 0.2 mg/mL collagenase A
707 (#10103578001, Roche) solution at a flow rate of 6 mL/min. The livers were mashed through
708 a 100 μm cell strainer and incubated in RPMI medium containing 25 mM HEPES, 0.4 mg/mL

collagenase A, and 10 U/mL DNaseI (#10104159001, Roche) for 20 min with agitation at 37°C. After filtration through a 100 μm cell strainer, the cell suspensions were centrifuged at 400 × g for 7 min and resuspended in ACK lysis buffer for 3 min to remove red blood cells. The cell suspensions were washed in PBS containing 2% FBS and filtered through a 100 μm cell strainer. The cell suspensions were centrifuged at 50 × g for 1 min to segregate the cell fractions as follows; the pellet and supernatant were collected as the hepatocyte fraction and leukocyte/LSEC/HSC fraction, respectively. This procedure was repeated three times. Both fractions were centrifuged at 400 × g for 7 min before FACS staining.

Flow cytometry and cell sorting

Cell-surface Fc receptors were blocked in anti-mouse CD16/32 antibody (1:250, #553141, BD Bioscience) for 20 min at 4 °C before staining with FACS antibodies. Subsequently, the primary antibodies were added. All antibodies, conjugates, lot numbers and dilution rates are listed in **Supplementary Table 1**. For Marco staining, cells were stained with a primary unconjugated antibody, followed by staining with a fluorophore-conjugated secondary antibody. The cells were incubated for 30 min at 4°C for staining, followed by washing in PBS containing 2% FBS. After centrifugation at 500 × g for 5 min, the cells were resuspended in autoMACS running buffer. For intracellular cytokine staining, cells were stimulated for 5 h with 50 ng/mL phorbol 12-myristate 13-acetate (Sigma-Aldrich) and 500 ng/mL ionomycin (Sigma-Aldrich) in the

presence of 10 μg/mL Golgistop (BD Bioscience). Cell surface markers were stained first. After washing with 2% FBS-containing PBS, fixation and permeabilisation were performed using an Intracellular Fixation and Permeabilisation Buffer set (eBioscience™), followed by intracellular cytokine staining. The cells were resuspended in autoMACS running buffer. Raw data were obtained using FACS Celesta (BD Biosciences, USA) or SH800 cell sorter (Sony, Japan) and analysed using FlowJo (BD Biosciences). Cell sorting was performed on the SH800 cell sorter. Gating strategies are shown in **Supplementary Fig. 7**.

Single-cell RNA sequencing

The 10× Genomics Chromium Controller was used to construct a single-cell RNA library and sequence the single-cell suspension following the protocol outlined in the Chromium Single Cell 3' Reagent Kit User Guide. We used the Chromium Next GEM Single Cell 3' Kit v3.1 (#PN-1000269; 10x Genomics), Chromium Next GEM Chip G Single Cell Kit (#PN-1000127; 10x Genomics), and Dual Index Kit TT Set A (#PN-1000215; 10× Genomics). According to the manufacturer's recommendations, approximately 2,000 live cells per sample were loaded onto the Chromium controller to generate 2,000 single-cell gel-bead emulsions for library preparation and sequencing. Oil droplets of encapsulated single cells and barcoded beads (GEMs) were subsequently reverse-transcribed in the Veriti Thermal Cycler (Thermo Fisher Scientific), resulting in cDNA tagged with a cell barcode and unique molecular index. Next,

cDNA was amplified to generate single-cell libraries according to the manufacturer's protocol. The Agilent Bioanalyzer High Sensitivity DNA assay (#5067-4626; Agilent) was used to quantify the cDNA before it was enzymatically fragmented, end-repaired, and polyA-tagged. Cleanup/size selection was performed on the amplified cDNA using SPRIselect magnetic beads (#B23317, Beckman-Coulter). Next, Illumina sequencing adapters were ligated to the size-selected fragments and purified using SPRIselect magnetic beads. Finally, sample indices were selected and amplified, followed by double-sided size selection using SPRIselect magnetic beads. The final library quality was assessed using the Agilent Bioanalyser High Sensitivity DNA assay. The samples were then sequenced on the Illumina NovaSeq 6000 in paired-end mode (read 1: 28 bp; read 2: 91 bp). The resulting raw reads were processed using 10× Genomics CellRanger 4.0.0.

Processing of single-cell RNA sequencing data

R (version 4.1.2) and Seurat (version 4.1.1) were used for processing the single-cell transcriptome data[70]. Unsupervised clustering and gene expression analysis were performed according to the Seurat guidance. In brief, we omitted the genes and cells in the data based on the following criteria: (1) the genes detected in fewer than five cells, (2) the cells with fewer than 200 or more than 5,000 genes, and (3) the cells with more than 20% mitochondrial genes. In mouse zone-specific single-cell RNA-seq, a total of 2,461 cells (including 1,282 cells and

766 1,179 cells from PV and CV zones, respectively) were selected for the subsequent analysis. In
767 a reanalysis of public human single-cell data, a total of 28,609 cells (including 16,786 and
768 11,823 cells from healthy and cirrhotic samples, respectively) were selected for the subsequent
769 analysis. Multiple data were integrated using the reciprocal principal components analysis
770 (RPCA)-based integration method, then linear dimensional reduction was performed using a
771 principal component analysis method. Cluster classification was performed using the nearest
772 neighbour graph-based clustering method, in which we tuned the dimensionality and resolution
773 parameters to determine the number of clusters. In the mouse analysis, 14 cell clusters were
774 initially obtained by setting the dimensionality to "1:15" and the resolution to "0.42." In the
775 human analysis, 14 cell clusters were initially obtained by setting the dimensionality to "1:15"
776 and the resolution to "0.2." Subsequently, we searched for marker genes for each cluster using
777 a 'FindAllMarkers' function and assign clusters to known cell types based on the markers
778 (**Supplementary Tables 2 and 3**) with reference to the previous reports[9,12,15,16,71–73]; however,
779 we omitted clusters that could not be assigned.
780
781 **Quantitative reverse transcription-polymerase chain reaction (qRT-PCR)**
782 Total RNA was extracted and purified using the RNeasy mini kit (#74106, Qiagen). cDNA was
783 prepared using Superscript III reverse transcriptase (#18080044, Invitrogen) following the
784 manufacturer's instructions. Real-time PCR was performed using TB Green Premix EX Taq

(#RR420W, TaKaRa) on a Thermal Cycler Dice Real Time System (TaKaRa, Japan). Relative gene expression levels were calculated by the ΔΔCt method using *Gapdh* as an internal control. The specific primer pairs (forward and reverse sequences, respectively) are listed in **Supplementary Table 4**. *Gapdh* is a broadly acceptable choice as one of the stable housekeeping genes for use in macrophages[74]. We also confirmed the validity of *Gapdh* by comparing the results with that of other commonly used internal control genes, *18s*, *Rpl32*, *B2m*, and *Ubc* (the data are shown in **Supplementary Fig. 8**). Furthermore, we validated the accuracy of the qPCR results by conducting a multimodal analysis.

Immunofluorescence staining and confocal imaging

The livers were embedded in 4% paraformaldehyde (PFA) (#158127, Sigma) solution overnight and then dehydrated using 15% and 30% sucrose solutions. The livers were cut into small pieces and embedded in Tissue-Tek O.C.T.™ Compound. Frozen sections (20 μm thickness) were cut using a CM3050S cryostat (Leica) and fixed on APS-coated slides (Matsunami). The sections were permeabilised in 0.5% tween-20 (#P1379, Sigma) solution for 20 min at RT and blocked in 4% bovine serum albumin (BSA) (#A6003, Sigma) solution for 60 min. Subsequently, the sections were stained with antibodies diluted in PBS containing 0.1% tween-20 and 1% BSA. The antibodies used for tissue staining are listed in **Supplementary Table 1**. After staining, the slides were mounted in PBS and scanned on a confocal microscope

(A1R, Nikon) with a ×20 objective lens (CFI Plan Apo VC, numerical aperture: 0.75, Nikon). Raw imaging data were processed using NIS elements (Nikon) and Imaris (Bitplane). Cell counting and cellular morphological analysis were performed using Imaris with the Spot and Surface functions, respectively.

16S rRNA-sequencing of colorectal bacteria

Colorectal contents were squeezed out from just below the cecum to the anus. The samples were instantly frozen with liquid nitrogen. DNA was extracted from the samples using GENE PREP STAR PI-1200 (Kurabo, Japan) according to the manufacturer's protocol. Each library was prepared according to the Illumina 16S Metagenomic Sequencing Library Preparation Guide with the primer set, 27Fmod: 5′AGRGTTTGATCMTGGCTCAG-3′ and 338R: 5′-TGCTGCCTCCCGTAGGAGT-3′, targeting the V1–V2 regions of the 16S rRNA gene. Next, 251-bp paired-end sequencing of the amplicons was performed on a MiSeq system (Illumina) using the MiSeq Reagent v2 500 cycle kit. The paired end sequences obtained were merged, filtered, and denoised using DADA2. Taxonomic assignment was performed using a QIIME2 feature-classifier plugin with the Greengenes 13_8 database. The QIIME2 pipeline[75], version 2020.2, served as the bioinformatics environment for the processing of all relevant raw sequencing data.

In vivo assay of MP2 Kupffer cell induction by Odoribacteraceae

To establish gnotobiotic mice, germ-free mice received 1×10^8 colony forming units (CFUs) of Odoribacteraceae (Odori) or *Bacteroides stercoris* (Stercoris) via oral gavage twice at days 0 and 2. Germ-free mice and gnotobiotic mice were then maintained in individual isolators, respectively, at the animal facilities of Oriental Bio Service, Inc. At day 21, the livers and colorectal contents of germ-free and gnotobiotic mice were harvested for the assays. For assessment of MP2 induction by SPF commensals or by combination of Odori/Stercoris and SPF commensals, mice were treated with ampicillin, vancomycin, neomycin, and metronidazole via drinking water for 6 weeks to deplete gut commensals and reduce MP2 population, and then Odori, Stercoris, or vehicle was inoculated into the mice. The mice were housed with SPF mice in the same cage. As for the inoculation of Odori and Stercoris, 1×10^8 CFUs of each bacterium was inoculated per mouse via oral gavage for the first 5 days consecutively, and thereafter, every other day until day 19. At day 21, the livers and colorectal contents were harvested for the assays.

Measurement of faecal isoallo-lithocholic acid concentration

Faecal contents were suspended in 10 times the volume of 2-propanol containing the internal standard (250 ng/mL LCA-d_4). The suspension was homogenised using Precellys (Bertin Technologies) and then incubated for 30 min at 37 °C under sonication. The suspension was

centrifuged at 13,000 × g for 5 min at 4 °C. Supernatant was collected for LC-MS/MS analysis. 1 μL of the supernatant was used for the analysis. LC-MS/MS analysis was performed under previously reported conditions[26] with slight modifications using a Nexera XR system (Shimadzu, Japan) coupled with an LCMS-8050 triple quadrupole mass spectrometer (Shimadzu) with a heated electrospray ionization source. A separation column, InertSustain C18 (150 mm × 2.1 mm I.D., 3 μm; GL Sciences), was used at 40 °C. A mixture of 10 mM ammonium acetate (A) and acetonitrile (B) was used as the mobile phase and the separation was carried out by gradient elution at a flow rate of 0.2 mL/min. The gradient condition was as follows: 14%B, 0–0.5 min; 14–22%B, 0.5–5 min; 22–28%B, 5–28 min; 28–54%B, 28–55 min; 54–98%B, 55–66 min; 98%B, 66–70 min; and 14%B, 70–75 min. To operate the LC-MS/MS analysis, we used the following MS parameters: interface voltage, -3kV; interface temperature, 300 °C; desolvation line temperature, 250 °C; heat block temperature, 400 °C; nebulizing gas, 2 L/min; heating gas, 10 L/min; drying gas, 10 L/min. A deuterated internal standard（LCA-d_4）was used to quantify isoallo-LCA. The data analysis was performed using LabSolutions, ver. 5.120 (Shimadzu).

Preparation of enhanced green fluorescent protein (eGFP)-labelled *E. coli* and in vivo challenges

We inserted eGFP DNA into multiple cloning sites of the bacterial vector pQE-60. *E. coli*

DH5α cells (#9057, TaKaRa) were transformed using this recombinant vector and then plated on lysogeny broth medium (#20069-65, Nacalai) containing 100 μg/mL ampicillin (#19769-64, Nacalai). Single eGFP-positive colonies were picked and further cultured in lysogeny broth medium (#20068-75, Nacalai) containing 100 μg/mL ampicillin with agitation at 37°C for propagation. The cell density of *E. coli* was measured using BioPhotometer Plus (Eppendorf, Germany) and adjusted to an OD600 of 0.38–0.40. The *E. coli* culture medium (1 mL) was collected and centrifuged at 10,000 × g for 5 min. The supernatant was discarded, and the pellet was suspended in sufficient PBS to remove any released bacterial components. Subsequently, the *E. coli* suspension was re-centrifuged at 10,000 × g for 5 min. The supernatant was discarded, and the pellet was resuspended in 500 μL PBS. Then, 100 μL of the suspension was slowly injected into the mice via the PV using an ultra-fine 29 G insulin syringe (#SS-10M2913A, TERUMO). Thereafter, the liver was immediately harvested and fixed in 4% PFA before immunofluorescence staining.

In vitro assay of bacterial capture by liver-resident macrophages

The eGFP-labelled *E. coli* density was measured using BioPhotometer Plus and adjusted to an OD600 of 0.19 – 0.21. The *E. coli* culture medium (1 mL) was collected, and 400 μL of an *E. coli*-containing PBS suspension was prepared as described above. Intrahepatic immune cells were collected from the liver (see above), and Kupffer cells were plated onto a 6-well glass-

bottom dish (#5816-006, Iwaki) in 3 mL Dulbecco's Modified Eagle Medium (#08459-64, Nacalai) containing 2% FBS and 10 ng/mL macrophage colony-stimulating factor (#315-02, Peprotech) at 37°C for 2 h to allow the Kupffer cells to adhere to the bottom. The cells were then washed to remove any non-adhering cells. The *E. coli* (150 μL) suspension was added to the Kupffer cells and incubated for 1 h at 37°C to allow the Kupffer cells to capture the *E. coli*. Subsequently, the cells were washed and incubated in cell dissociation Hank's solution (#S-004-B, Millipore) for 10 min at 37°C for collection. The cells were then stained with CD45-PE/Cy7, CD64-PerCP/Cy5.5, F4/80-APC, and MARCO-DyLight405 (see **Supplementary Table 1**) and analysed using BD FACS Celesta and FlowJo software.

Experimental colitis model

The mice received 1% dextran sodium sulphate (DSS, #160110, MP Biomedicals) via drinking water for 7 days, followed by untreated normal water for 4 days to induce acute colitis[76]. The mice were used for the assays 11 days after starting DSS treatment. Mouse body weights were measured on days 0, 7, and 11. To generate the chronic colitis model, the mice received three cycles of 1% DSS via drinking water for 7 days, followed by untreated normal water for 7 days[77]. After the third DSS treatment, normal water was given for 4 days. The livers were harvested for the assays 39 days after the start of the first DSS treatment. Mouse body weights were measured on days 0, 7, 14, 21, 28, 35, and 39.

899

900 **Diet-induced NAFLD/NASH model**

901 Mice were fed ad libitum for up to 8 weeks with a 0.1 % methionine and choline-deficient
902 high-fat (60 kcal%) diet[78,79] (Research Diets, A06071302) to induce the non-alcoholic fatty
903 liver disease and steatohepatitis (NAFLD/NASH). Peripheral blood and livers were harvested
904 every 2 weeks for the assays. Serum samples were prepared for the biochemical analyses. Liver
905 samples were fixed in 4 % paraformaldehyde for 2 days. Some parts were embedded in paraffin,
906 and the others were dehydrated with 15% and 30% sucrose solutions and embedded in O.C.T.
907 Compound. Paraffin-embedded livers were used for Masson trichrome staining and O.C.T.
908 Compound-embedded frozen livers were used for immunofluorescence staining.

909

910 **Human samples and immunofluorescence staining**

911 The Institutional Review Board for Clinical Research at Osaka University Hospital approved
912 this study. Informed consent for surgical intervention was obtained from each patient. Control
913 or PSC liver tissues, located far from any colorectal cancer metastatic lesion, were obtained
914 from patients who underwent surgical resection at Osaka University Hospital. These tissue
915 specimens were immediately fixed in 10% formalin and then processed routinely for paraffin
916 embedding. Paraffin-embedded sections were cut at a thickness of 4 μm, deparaffinised in
917 cresol and ethanol, and rinsed in PBS. Antigens were retrieved by heating with EnVision FLEX

Target Retrieval Solution, High pH (Dako, Agilent) at 110 °C for 15 min. After washing in deionised distilled water and EnVision FLEX Wash Buffer (Dako, Agilent), the sections were incubated in Antibody Diluent/Block (Akoya Biosciences) for 30 min at RT. Primary antibodies were diluted in the Antibody Diluent/Block. After incubation with antibodies at 4 °C overnight, the sections were washed in Wash Buffer, incubated with Opal Polymer HRP Ms + Rb (Akoya Biosciences) for 30 min at RT, and washed in Wash Buffer. Next, the sections were incubated with Opal fluorophores (Akoya Biosciences) for 10 min, then washed in Wash Buffer and rinsed in PBS. For the subsequent antibody applications, the slides were heated again to remove the antibody complexes after incubation, followed by the steps described above. Finally, after heating, the slides were washed with Wash Buffer and then cover-slipped in Fluoro-KEEPER Antifade Reagent, Non-Hardening Type with DAPI (Nacalai Tesque). The primary antibodies used included anti-MARCO (Sigma-Aldrich) (1:500 dilution), anti-CD68 (Dako, Agilent) (1:100 dilution), and anti-CK19 (Cell Marque) (1:100 dilution). The fluorophores used included Opal 690, Opal 570, and Opal 520 at 1:100 dilution in 1 × Plus Amplification Diluent (Akoya Biosciences). Imaging was performed using a confocal microscope (A1R, Nikon) with a ×20 objective lens (CFI Plan Apo VC, numerical aperture: 0.75, Nikon). The antibodies used for human tissue staining are listed in **Supplementary Table 1**.

Statistics and Reproducibility

All line graphs are presented as means ± standard error of the mean (SEM). All box plots present the means, medians, smallest observations, lower and upper quartiles, and largest observations. Basically, nonparametric paired and unpaired two-sided Mann–Whitney U tests were applied for comparisons between the two groups. Statistical analyses were performed using R (version 4.1.2). Experiments were repeatedly performed to ensure the reproducibility of our observations. All results were determined from at least two independent experiments (twice: Figs. 1e-h, 2a, 4a-d, f, Extended Data Figs. 5a-h, 6a-h, 7a-c, 10a-c, 11b-d, g-j, Supplementary Figs. 1a-c, 2a-c, 3d, 8a-d, and three or more times: Figs. 1a-d, i, 2b-d, 3a-f, 4e, g, h, 5b-i, Extended Data Figs. 1a, b, 2c-e, 4a-c, 7e, f, 8b-e, 9b-p, 11f, Supplementary Figs. 2d, e, 3c, 4a-d, 5a-c).

Data availability

Visium and single-cell RNA sequencing data have been deposited in the NCBI Gene Expression Omnibus (GEO) database under the accession numbers GSE213388 and GSE213165 [https://www.ncbi.nlm.nih.gov/geo/query/acc.cgi], respectively. For the reanalysis of mouse liver single-cell RNA sequencing and Visium, we obtained the datasets from the GEO (the accession number: GSE192742 and URL: https://www.ncbi.nlm.nih.gov/geo/query/acc.cgi)[9]. For the reanalysis of human single-cell RNA sequencing, we obtained the data of human liver $CD45^+$ cells from eight patients (four

normal and four cirrhotic livers) from the GEO (the accession numbers: GSM4041150, GSM4041153, GSM4041155, GSM4041160, GSM4041161, GSM4041166, GSM4041168, GSM4041169 and URL: https://www.ncbi.nlm.nih.gov/geo/query/acc.cgi?acc=GSE136103)[15]. For the reanalysis of mouse liver and intestine single-cell RNA sequencing, we obtained the datasets from Mouse Cell Atlas[80] [https://bis.zju.edu.cn/MCA/]. All other data in this study are available from the corresponding author upon reasonable request.

Code availability

All source codes for the Visium and single-cell analyses are available from the GitHub repository [https://github.com/OU-ICB/YMiyamoto2023].

966 **Methods references**

967 51. Adachi, O. *et al.* Targeted disruption of the MyD88 gene results in loss of IL-1- and IL-
968 18-mediated function. *Immunity* **9**, 143–150 (1998).

969 52. Victora, G. D. *et al.* Germinal center dynamics revealed by multiphoton microscopy
970 with a photoactivatable fluorescent reporter. *Cell* **143**, 592–605 (2010).

971 53. Madisen, L. *et al.* A robust and high-throughput Cre reporting and characterization
972 system for the whole mouse brain. *Nat. Neurosci.* **13**, 133–140 (2010).

973 54. Arredouani, M. *et al.* The scavenger receptor MARCO is required for lung defense
974 against pneumococcal pneumonia and inhaled particles. *J. Exp. Med.* **200**, 267–272
975 (2004).

976 55. Atarashi, K. *et al.* Induction of colonic regulatory T cells by indigenous Clostridium
977 species. *Science* **331**, 337–341 (2011).

978 56. Faust, N., Varas, F., Kelly, L. M., Heck, S. & Graf, T. Insertion of enhanced green
979 fluorescent protein into the lysozyme gene creates mice with green fluorescent
980 granulocytes and macrophages. *Blood* **96**, 719–726 (2000).

981 57. Jung, S. *et al.* Analysis of fractalkine receptor CX_3CR1 function by targeted deletion
982 and green fluorescent protein reporter gene insertion. *Mol. Cell. Biol.* **20**, 4106–4114
983 (2000).

984 58. Kamran, P. *et al.* Parabiosis in mice: a detailed protocol. *J. Vis. Exp.* 1–5 (2013).

985 59. Tavares, A. J. *et al.* Effect of removing Kupffer cells on nanoparticle tumor delivery.
986 *Proc. Natl. Acad. Sci. U. S. A.* **114**, E10871–E10880 (2017).
987 60. Xu, M. *et al.* c-MAF-dependent regulatory T cells mediate immunological tolerance to
988 a gut pathobiont. *Nature* **554**, 373–377 (2018).
989 61. Ogawa, Y. *et al.* Gut microbiota depletion by chronic antibiotic treatment alters the
990 sleep/wake architecture and sleep EEG power spectra in mice. *Sci. Rep.* **10**, 19554
991 (2020).
992 62. Hie, B., Bryson, B. & Berger, B. Efficient integration of heterogeneous single-cell
993 transcriptomes using Scanorama. *Nat. Biotechnol.* **37**, 685–691 (2019).
994 63. Wolf, F. A., Angerer, P. & Theis, F. J. SCANPY: large-scale single-cell gene expression
995 data analysis. *Genome Biol.* **19**, 15 (2018).
996 64. Huang, D. W., Sherman, B. T. & Lempicki, R. A. Systematic and integrative analysis
997 of large gene lists using DAVID bioinformatics resources. *Nat. Protoc.* **4**, 44–57 (2009).
998 65. Schneider, C. A., Rasband, W. S. & Eliceiri, K. W. NIH Image to ImageJ: 25 years of
999 image analysis. *Nat. Methods* **9**, 671–675 (2012).
1000 66. Lämmermann, T. *et al.* Neutrophil swarms require LTB4 and integrins at sites of cell
1001 death in vivo. *Nature* **498**, 371–375 (2013).
1002 67. Uderhardt, S., Martins, A. J., Tsang, J. S., Lämmermann, T. & Germain, R. N. Resident
1003 macrophages cloak tissue microlesions to prevent neutrophil-driven inflammatory

damage. *Cell* **177**, 541-555 (2019).

68. Medaglia, C. *et al.* Spatial reconstruction of immune niches by combining photoactivatable reporters and scRNA-seq. *Science* **358**, 1622–1626 (2017).

69. Bonnardel, J. *et al.* Stellate cells, hepatocytes, and endothelial cells imprint the Kupffer cell identity on monocytes colonizing the liver macrophage niche. *Immunity* **51**, 638-654 (2019).

70. Hao, Y. *et al.* Integrated analysis of multimodal single-cell data. *Cell* **184**, 3573-3587 (2021).

71. Xiong, X. *et al.* Landscape of intercellular crosstalk in healthy and NASH liver revealed by single-cell secretome gene analysis. *Mol. Cell* **75**, 644-660 (2019).

72. Aizarani, N. *et al.* A human liver cell atlas reveals heterogeneity and epithelial progenitors. *Nature* **572**, 199–204 (2019).

73. Liew, P. X., Lee, W.-Y. & Kubes, P. iNKT cells orchestrate a switch from inflammation to resolution of sterile liver injury. *Immunity* **47**, 752-765 (2017).

74. Ju, W. *et al.* Reference gene selection and validation for mRNA expression analysis by RT-qPCR in murine M1- and M2-polarized macrophage. *Mol. Biol. Rep.* **47**, 2735–2748 (2020).

75. Bolyen, E. *et al.* Reproducible, interactive, scalable and extensible microbiome data science using QIIME 2. *Nat. Biotechnol.* **37**, 852–857 (2019).

76. Mathies, F. *et al.* Colitis promotes a pathological condition of the liver in the absence of Foxp3^{+} regulatory T cells. *J. Immunol.* **201**, 3558–3568 (2018).

77. Kwon, J., Lee, C., Heo, S., Kim, B. & Hyun, C.-K. DSS-induced colitis is associated with adipose tissue dysfunction and disrupted hepatic lipid metabolism leading to hepatosteatosis and dyslipidemia in mice. *Sci. Rep.* **11**, 5283 (2021).

78. Matsumoto, M. *et al.* An improved mouse model that rapidly develops fibrosis in non-alcoholic steatohepatitis. *Int. J. Exp. Pathol.* **94**, 93–103 (2013).

79. Ikawa-Yoshida, A. *et al.* Hepatocellular carcinoma in a mouse model fed a choline-deficient, L-amino acid-defined, high-fat diet. *Int. J. Exp. Pathol.* **98**, 221–233 (2017).

80. Fei, L. *et al.* Systematic identification of cell-fate regulatory programs using a single-cell atlas of mouse development. *Nat. Genet.* **54**, 1051–1061 (2022).

Acknowledgments

We appreciate Dr. Ronald N. Germain (NIAID/NIH, Maryland, USA) for critically reviewing the manuscript. We thank Drs. Y. Yahara, S. Kameoka, F. Sugihara, T. Sudo, T. Ariyoshi, Bo Li, and Ms. M. Shirazaki, Ms. F. Okiji, Ms. A. Sakai for their instructive comments and technical assistances. This work was supported by CREST (JPMJCR15G1 to M.I.) from Japan Science and Technology (JST) Agency; Grant-in-Aid for Scientific Research (S) (19H05657 to M.I.), for Transformative Research Areas (A) (20H05901 to M.I.), for International Leading Research (22K21354 to M.I.), for JSPS Fellows (21J13888 to Y.M.) and Research Activity Start-up (22K20760 to Y.M.) from the Japan Society for the Promotion of Science (JSPS); the Innovative Drug Discovery and Development Project (JP21am0401009 to M.I.) and the Program on the Innovative Development and the Application of New Drugs for Hepatitis B (JP23fk0310512 to M.I.) from Japan Agency for Medical Research and Development (AMED); and Uehara Memorial Foundation (to M.I.). Cartoons in this manuscript were created using Biorender.com. We would like to thank Editage (www.editage.jp) for English language editing.

Author contributions

Y.M. conceived the original idea of this study. Y.M. and M.I. devised the concrete concept. Y.M., J.Kikuta, and M.I. designed the experiments. Y.M. conducted all of the experiments and

data analyses with assistance from J.Kikuta, T.M., T.H., K.F., Y.U. and E.Y. D.M. and D.O. processed the sequence data. Y.C.L., S.S. and D.O. established a new data processing method for spatial transcriptomics. S.K. and H.E. collected and provided the human liver samples and T.M. and E.M. performed the immunofluorescence staining. K. Tryggvason generated *Marco*$^{-/-}$ mice. T.S. maintained them and assisted with experiments using *Marco* knockout mice. K.A. and K.H. isolated and provided *Odoribacteraceae* Strain#21. T.Y. and J.Kunisawa measured concentrations of isoallo-lithocholic acid in faeces. H.K. and K. Takeda supervised the experiments and analyses pertaining to gut commensal microbes. Y.M. wrote the initial draft, and Y.M., J.Kikuta and M.I. revised the final draft.

Competing interests

The authors declare no competing financial interests.

Additional information

Supplementary Information is available for this paper.

Correspondence and requests for materials should be addressed to Masaru Ishii (**mishii@icb.med.osakau.ac.jp**)

Extended Data Figure Legends

Extended Data Fig. 1. Spatial heterogeneity in neutrophil adhesion in the steady-state liver. a, Representative intravital image [left, green: neutrophils, red: Qtracker655 (blood vessels), and blue: SHG (tissue collagens)] and neutrophil tracks (right, individual colours mean individual cell tracks). Tracks of neutrophils that adhered to the tissue for over 10 min are shown. Scale bar: 100 μm. **b**, Numbers of the neutrophil tracks within each zones (n = 7). The quantitative data are presented as means (asterisk) with medians, smallest observations, lower and upper quartiles, and largest observations. Statistical significance was determined using unpaired two-sided Mann–Whitney U test.

Extended Data Fig. 2. Spatial heterogeneity in monocyte/macrophage responses to the laser-induced tissue damage in the liver. a, Timeline of neutrophil and monocyte responses post the laser-induced tissue damage. **b**, Experimental design to quantify monocyte/macrophage accumulations at the laser-induced damaged sites. **c**,**d**, Representative intravital images of in situ inflammatory responses by monocytes/macrophages upon the laser-induced damages under control (c, n = 13) and clodronate liposome-treated (resident macrophage-depleted) conditions (d, n = 10) [green: monocytes/macrophages, white: damaged sites (autofluorescence), and blue: SHG (tissue collagens)]. Scale bar: 100 μm. Quantified accumulation scores of monocyte/macrophage at the lesions are shown (right). **e**, PV/CV ratio of monocyte/macrophage accumulation at 24 h post-laser ablation under control (n = 13) and resident macrophage-depleted (n = 10) conditions, indicating spatial polarisation of accumulation: > 1 and < 1 indicate bias towards PV and CV zones, respectively. All quantitative data are presented as means (asterisk) with medians, smallest observations, lower and upper quartiles, and largest observations. Statistical significance was determined using paired (**c, d**) and unpaired (**e**) two-sided Mann–Whitney U tests.

Extended Data Fig. 3. Reanalysis to identify the Marco$^+$ Kupffer cell subset (MP2) using public mouse and human databases. a, Reproduction of Uniform Manifold Approximation and Projection (UMAP) depicting distinct myeloid cell clusters identified in the mouse liver cell atlas. The Kupffer cell cluster was further analysed for isolating subclusters. **b**, Density of *Marco*- (left) and *Il10*- (right) expressing cells in each Kupffer cell subcluster. Subclusters 8, 10 and 17 should be the MP2. **c**, Reproduction of UMAP depicting the liver zonation in the mouse liver cell atlas. **d**, Density of *Marco*$^+$ *Clec4f*$^+$ spots on the liver zonation plot (left). Violin plot showing quantification of the densities in each zone (right). Statistical significance was determined using one-sided Student's t-test and resultant *p*-values were corrected using the Benjamini-Hochberg method. **e**, Summary of human sample information (left). tSNE plot depicting distinct immune cell clusters (right). All single-cell data from healthy and cirrhotic samples were integrated and represented on the same tSNE plot. Each cluster was assigned to the known cell types based on marker genes (**Supplementary Table 3**). The numbers in brackets indicate the cluster number. Resident macrophages include three clusters. **f**, Gene expression of *CD68* (left), a human macrophage marker, *MARCO* (centre), and *IL10* (right) was visualised with an R package 'Nebulosa' (Kernel Gene-Weighted Density Estimation). **g**, Percentage of MARCO$^+$ IL10$^+$ cells to total macrophages under healthy and cirrhotic conditions. Data are presented as means (asterisk) with medians, smallest observations, lower

and upper quartiles, and largest observations. Statistical significance was determined using unpaired two-sided Mann–Whitney U test.

Extended Data Fig. 4. Relationship between Marco and IL-10 expressions in Kupffer cells. **a**, Transcriptional activity of *Il10* in Marco^{-} (MP1) and Marco^{+} (MP2) Kupffer cells visualised using *Il10*-Venus mice (n = 7). To confirm the background noise, we used wild-type mice as the negative control (n = 5). Venus expression was detected using AlexaFluor647-conjugated anti-Venus antibody to avoid the influence of autofluorescence. Mean fluorescence intensity (MFI) of AlexaFluor647 (from *Il10*-venus) was measured for statistical comparison. **b**, Correlation between Marco and Il10-venus expressions. 'R' indicates the correlation coefficient. The error bands mean 95% confidence interval. **c**, Relative mRNA expression of *Il10*, *Il1rn* and *Tgfb1* to *Gapdh* in total Kupffer cell fraction from *Marco*$^{+/+}$ control (n = 7-9) and *Marco*$^{-/-}$ (n = 5-9) mice. All data are presented as means (asterisk) with medians, smallest observations, lower and upper quartiles, and largest observations. Statistical significance was determined using unpaired two-sided Mann–Whitney U test.

Extended Data Fig. 5. Interleukin-10 signalling in PV zones suppressively regulates ICAM1-integrin interactions between endothelial cells and neutrophils. a, Representative flow cytometry gating to identify the liver sinusoidal endothelial cell (LSEC) subsets. The histogram shows the ICAM-1 expression levels on each subset. **b**, Mean fluorescence intensity (MFI) from ICAM-1 on $CD117^+$ and $CD117^-$ LSECs (n = 4). **c**, Representative immunofluorescence images of ICAM-1 in the liver tissue (n = 4, blue: E-cadherin$^+$ PV zones, green: ICAM-1). PV, portal vein; CV, central vein. Scale bar : 100 µm. **d**, MFI from ICAM-1 on $CD117^+$ and $CD117^-$ LSECs under anti-IL10R and isotype control antibody-treated conditions (n = 9 and 7, respectively). **e**, Fold changes of *Cxcl1* and *Cxcl2* mRNA expressions to *Gapdh* in $CD117^+$ LSECs, $CD117^-$ LSECs, and Kupffer cells from anti-IL10R and isotype control antibody-treated mice (n = 7 and 6, respectively). Data were standardized to ensure a control group mean value of '1'. **f–h**, Analyses of infiltrating neutrophils in the liver under anti-IL10R and isotype control antibody-treated conditions (n =4, respectively). Representative staining of integrin αM (Mac-1 or CD11b) on $CD45^+$ Mac-1^+ Ly-$6G^+$ neutrophils (f), percentage of Mac-1^{high} neutrophils (g), and absolute number of neutrophils (h). All data are presented as means (asterisk) with medians, smallest observations, lower and upper quartiles, and largest observations. Statistical significance was determined using unpaired two-sided Mann–Whitney U test.

Extended Data Fig. 6. In vitro and in vivo assays of *E. coli*-capturing activity of MP1 and MP2 Kupffer cells. **a**, Experimental design for in vitro bacteria-capture assay. **b**, Representative flow cytometry gating for identifying Marco$^-$ (MP1) and Marco$^+$ (MP2) Kupffer cells, and comparison of *E. coli*-derived fluorescence signals. **c**, Mean fluorescence intensity (MFI) of *E. coli*-derived GFP signals in MP1 and MP2 (n = 7). **d**, Experimental design for in vivo bacteria-capture assay. **e**, Representative immunofluorescence images (n = 3, 9 visual fields, white: *E. coli*, red: F4/80$^+$ macrophages, blue: E-cadherin$^+$ PV zones) showing *E. coli* localisation in the liver (left and centre). Scale bar: 100 μm. Percentage of *E. coli* numbers within each zone to total *E. coli* (right). The exact *p*-value is 4.114×10^{-5}. **f**, Representative immunofluorescence images (n = 3, 15 visual fields, white: *E. coli*, blue: Marco$^-$ MP1, and red: Marco$^+$ MP2) showing the *E. coli*-capturing capability of each subset (left). The raw images were processed using the Imaris software (centre, yellow: *E. coli*, blue: Marco$^-$ MP1, and red: Marco$^+$ MP2). Scale bar: 100 μm. Percentage of *E. coli*-capturing Marco$^-$ MP1 and Marco$^+$ MP2 to total *E. coli*-capturing cells (right). **g**, Percentage of cells engulfing more than two *E. coli* in each Kupffer cell subset. **h**, Representative images showing *E. coli* localisation in the *Marco*$^{+/+}$ (n = 5, 25 visual fields) and *Marco*$^{-/-}$ (n = 4, 30 visual fields) livers (left, yellow: *E. coli*, blue: E-cadherin$^+$ PV zones). *E. coli* are shown as spherical spots using the imaris. Scale bar: 100 μm. Percentage of *E. coli* numbers within each zone to total *E. coli*

(right). The exact *p*-values are 1.376×10^{-6} (PV) and 1.376×10^{-6} (CV). Data are presented as means (asterisk) with medians, smallest observations, lower and upper quartiles, and largest observations. Statistical significance was determined using paired (c) and unpaired (e-h) two-sided Mann–Whitney U test.

Extended Data Fig. 7. Identification of gut commensal bacteria that induce MP2 Kupffer cells and involvement of gut commensals in MP2 induction by isoallo-lithocholic acids. a, Relative abundance (%) of microbes at the family level (n = 6 and 5 for the SPF-A and SPF-B groups, respectively). The data were obtained by 16S rRNA-sequencing. **b**, Relative abundance (%) of each bacterium significantly enriched in "SPF-A" colorectal contents (n = 6 and 5 for the SPF-A and SPF-B groups, respectively). **c**, Correlation between the relative abundance of bacterium and the percentage of Marco^{+} Kupffer cells (MP2). 'R' indicates the correlation coefficient. **d**, Graphical protocol for isoallo-lithocholic acid (isoalloLCA) and/or antibiotic treatments. **e**, Percentage of Marco^{+} cells to total Kupffer cells under DMSO (n = 10), isoalloLCA (n = 10), and antibiotic/isoalloLCA (n = 13) treatments. **f**, Fold changes of *Il10* mRNA expression in total Kupffer cells under each condition [DMSO (n = 10), isoalloLCA (n = 10), and antibiotics/isoalloLCA (n = 9)]. Data were standardized to ensure a control group mean value of '1'. All data are presented as means (asterisk) with medians, smallest observations, lower and upper quartiles, and largest observations. Statistical significance was determined using unpaired two-sided Mann–Whitney U test.

Extended Data Fig. 8. Periportal immunosuppressive Kupffer cells protect against gut commensal-driven liver inflammation related to experimental colitis. a, Experimental

design; *Marco*$^{+/+}$ and *Marco*$^{-/-}$ mice received 1% dextran sodium sulphate (DSS) via drinking water for 7 days to induce acute colitis, followed by drinking normal water for 4 days for recovery. On day 11, the livers were harvested for assays. **b**, Relative mRNA expression of anti-inflammatory cytokines *Il10* and *Il1rn* in Kupffer cells from *Marco*$^{+/+}$ and *Marco*$^{-/-}$ mice (n = 6 each). **c**, Representative intravital images of infiltrating inflammatory neutrophils in *Marco*$^{+/+}$ (left) and *Marco*$^{-/-}$ (right) mice (n = 6 each, green: neutrophils, red: vascular structures visualised by Qtracker655). Scale bar: 100 μm. **d**, Quantification of neutrophil numbers in 100 μm^3 tissues (n = 6, 12 visual fields per condition). Data contain two tissue sections from different lobes per mouse. **e**, Body weight change showing the percentage of body weight on day 11 to the original body weight (on day 0) (n = 6 each). All quantitative data are presented as means (asterisk) with medians, smallest observations, lower and upper quartiles, and largest observations. Statistical significance was determined using unpaired two-sided Mann–Whitney U test.

Extended Data Fig. 9. Periportal immunosuppressive Kupffer cells suppress progression of the non-alcoholic fatty liver disease. a, Analysis schedule. **b**, Representative Marco and TIM-4 staining in $CD45^+$ CX_3CR1^- $F4/80^+$ $CD64^+$-gated macrophages. **c,d,f,h**, Kinetics of the frequency of $Marco^+$ TIM-4^+ MP2 Kupffer cells (c), serum AST (d), serum ALT (f), and neutrophil abundance (h) [Healthy (n = 6-7), NAFLD/NASH 2W (n = 9-12), 4W (n = 11-12) and 6W (n = 8)]. **e**,**g**,**i**, Correlation between MP2 frequency and AST (e), ALT (g), and neutrophil abundance (i) in NAFLD/NASH 2W. 'R' indicates the correlation coefficient. The error bands mean 95% confidence interval. **j**, Serum AST and ALT levels in NAFLD/NASH-induced *Marco*$^{+/+}$ (n = 12, 12, 8 for 2W, 4W, 6W, respectively) and *Marco*$^{-/-}$ mice (n = 8, 10, 8 for 2W, 4W, 6W, respectively). **k**, Representative Masson trichrome staining of healthy *Marco*$^{+/+}$, NAFLD/NASH-induced *Marco*$^{+/+}$ and *Marco*$^{-/-}$ livers. Scale bar: 200 μm. **l**, Percentage of area occupied by fat droplets around portal veins in NAFLD/NASH 6W: *Marco*$^{+/+}$ (n = 5, 8 visual fields) and *Marco*$^{-/-}$ (n = 5, 10 visual fields). **m**, AST/ALT ratio in NAFLD/NASH 6W: *Marco*$^{+/+}$ and *Marco*$^{-/-}$ mice (n = 8 each). **n**, Representative immunofluorescence images showing MARCO (green), CD68 (red), and CK19 (cyan) in human livers: NAFLD/NASH (n = 7, 21 visual fields) and normal controls (n = 9, 27 visual fields). Scale bar: 100 μm. **o**, Absolute numbers of CD68-positive cells (macrophages) per visual field. **p**, Percentage of Marco-positive cells to total macrophages. All curve graphs

represent means ± standard error of the mean (SEM). All box plots represent means (asterisk) with medians, smallest observations, lower quartiles, upper quartiles, and largest observations. Statistical significance was determined using unpaired two-sided Mann–Whitney U test. The exact *p*-values are 3.969×10^{-5} (h), 7.693×10^{-5} (p, Normal vs NAFLD), 5.114×10^{-10} (p, Normal vs NASH).

Extended Data Fig. 10. Marco^{+} Kupffer cells (MP2) belong to the CD206^{-} ESAM^{-} KC1 subset. a, Representative staining of CD206 and ESAM on Marco^{+} and Marco^{-} Kupffer cells (CD45^{+} CX$_3$CR1^{-} F4/80^{+} CD64^{+} population). **b**, Percentage of Marco^{+} cells in KC1 and KC2 (n = 4). **c**, Percentage of total Marco^{+} Kupffer cells, Marco^{+} KC1, and Marco^{+} KC2 in all Kupffer cells (n = 4). **d**, Diagram illustrating the relationship between KC1/KC2 and MP1/MP2 classifications of Kupffer cells. All box plots represent means (asterisk) with medians, smallest observations, lower quartiles, upper quartiles, and largest observations. Statistical significance was determined using unpaired two-sided Mann–Whitney U test.

Extended Data Fig. 11. Marco$^+$ immunosuppressive Kupffer cells are supplied by embryo-derived macrophages. a, Experimental design; generating a parabiosis model to examine the differentiation from bone marrow-derived monocytes into Marco$^+$ Kupffer cells (MP2). **b**, Representative flow cytometry gating of tdTomato$^+$ cells on CD45$^+$ CX$_3$CR1$^-$ F4/80$^+$ CD64$^+$ cells in the liver from wild-type parabionts (left). Percentages of Marco$^-$ (MP1) and Marco$^+$ (MP2) cells to Tomato$^+$ Kupffer cells (right, n = 7). **c**, Representative immunofluorescence images of a wild-type parabiont liver [blue: E-cadherin (PV zones), white: tdTomato (bone marrow-derived macrophages), red: F4/80 (Kupffer cells), and green: Marco (MP2)]. Scale bar: 100 µm (large image) and 20 µm (zoomed images). **d**, Representative immunofluorescence images of a wild-type parabiont liver [white: tdTomato (bone marrow-derived macrophages), red: CD68 (Kupffer cells), and green: TIM-4 (resident Kupffer cells)]. Scale bar: 100 µm. **e**, Graphical protocol for analysing resident and bone marrow-derived (repopulated) Kupffer cells. **f**, Representative gating of Kupffer cells in clodronate liposome (CLL)-treated (on day 2) and untreated mice (left). Absolute number of TIM-4$^+$ resident Kupffer cells [right, control (n = 7) and CLL-treated (n = 6)]. **g**, Representative staining of Marco and TIM-4 on Kupffer cells in CLL-treated (on week 6) and untreated control mice. **h**, Absolute numbers of TIM-4$^+$ resident Kupffer cells (left) and TIM-4$^-$ bone marrow-derived Kupffer cells (right) in CLL-treated (on week 6, n = 12) and untreated control (n = 7) mice. The exact *p*-value is 3.969×10^{-5}. **i**,

Percentage of Marco^{+} cells in TIM-4^{+} and TIM-4^{-} Kupffer cells in CLL-treated mice (on week 6, n = 12). **j**, Relative mRNA expression of *Il10* to *Gapdh* in TIM-4^{+} and TIM-4^{-} Kupffer cells from CLL-treated mice (on week 6, n = 8). All data are presented as means (asterisk) with medians, smallest observations, lower and upper quartiles, and largest observations. Statistical significance was determined using unpaired (b, f, h) and paired (i, j) two-sided Mann–Whitney U test.

Figure 1

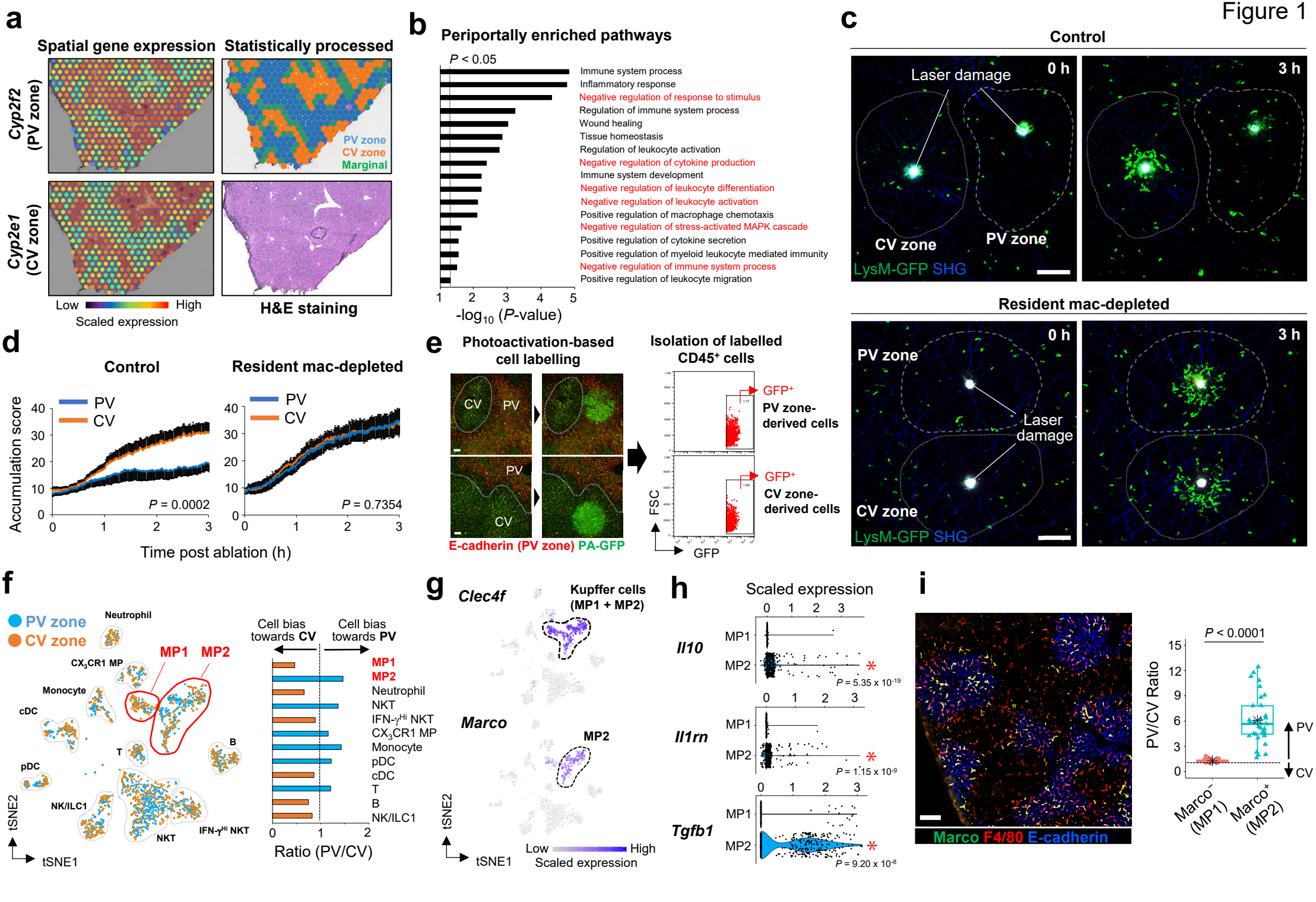
a
Spatial gene expression
Statistically processed
Cyp2f2 (PV zone)
Cyp2e1 (CV zone)
PV zone
CV zone
Marginal
Low
High
Scaled expression
H&E staining
b
Periportally enriched pathways
P < 0.05
Immune system process
Inflammatory response
Negative regulation of response to stimulus
Regulation of immune system process
Wound healing
Tissue homeostasis
Regulation of leukocyte activation
Negative regulation of cytokine production
Immune system development
Negative regulation of leukocyte differentiation
Negative regulation of leukocyte activation
Positive regulation of macrophage chemotaxis
Negative regulation of stress-activated MAPK cascade
Positive regulation of cytokine secretion
Positive regulation of myeloid leukocyte mediated immunity
Negative regulation of immune system process
Positive regulation of leukocyte migration
-log10 (P-value)
c
Control
Laser damage
0 h
3 h
CV zone
PV zone
LysM-GFP SHG
Resident mac-depleted
0 h
3 h
PV zone
Laser damage
CV zone
LysM-GFP SHG
d
Control
Resident mac-depleted
PV
CV
Accumulation score
P = 0.0002
P = 0.7354
Time post ablation (h)
e
Photoactivation-based cell labelling
Isolation of labelled CD45+ cells
CV
PV
E-cadherin (PV zone) PA-GFP
GFP+
PV zone-derived cells
CV zone-derived cells
FSC
GFP
f
PV zone
CV zone
Neutrophil
MP1
MP2
CX3CR1 MP
Monocyte
cDC
T
B
pDC
NK/ILC1
NKT
IFN-γHi NKT
tSNE2
tSNE1
Cell bias towards CV
Cell bias towards PV
MP1
MP2
Neutrophil
NKT
IFN-γHi NKT
CX3CR1 MP
Monocyte
pDC
cDC
T
B
NK/ILC1
Ratio (PV/CV)
g
Clec4f
Kupffer cells (MP1 + MP2)
Marco
MP2
tSNE2
tSNE1
Low
High
Scaled expression
h
Scaled expression
Il10
Il1rn
Tgfb1
MP1
MP2
P = 5.35 x 10-19
P = 1.15 x 10-9
P = 9.20 x 10-8
i
Marco F4/80 E-cadherin
P < 0.0001
PV/CV Ratio
PV
CV
Marco- (MP1)
Marco+ (MP2)

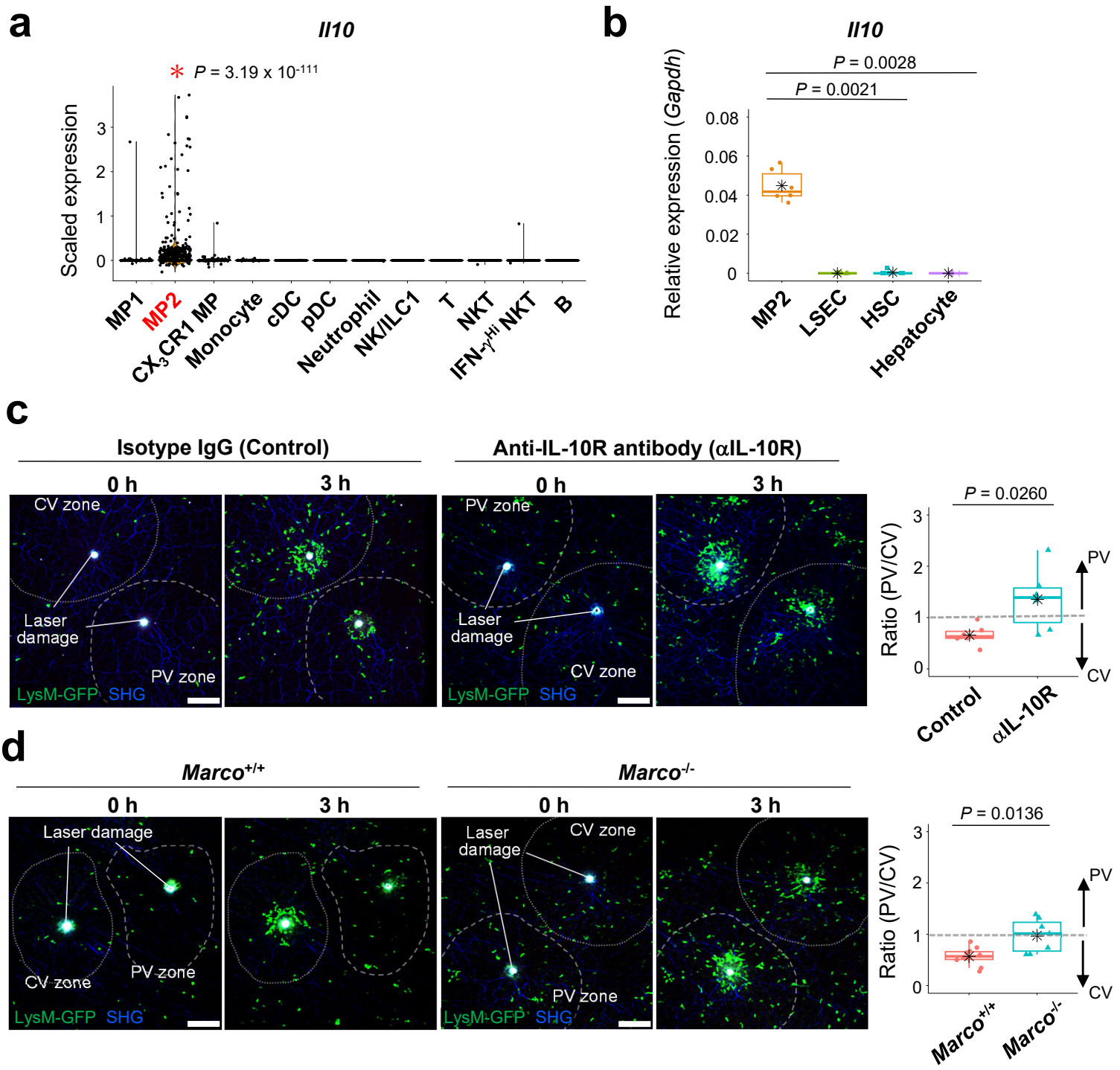
a
Il10
P = 3.19 x 10-111
Scaled expression
MP1
MP2
CX3CR1 MP
Monocyte
cDC
pDC
Neutrophil
NK/ILC1
T
NKT
IFN-γHi NKT
B
b
Il10
P = 0.0028
P = 0.0021
Relative expression (Gapdh)
MP2
LSEC
HSC
Hepatocyte
c
Isotype IgG (Control)
Anti-IL-10R antibody (αIL-10R)
0 h
3 h
CV zone
PV zone
Laser damage
LysM-GFP SHG
P = 0.0260
Ratio (PV/CV)
PV
CV
Control
αIL-10R
d
Marco+/+
Marco-/-
P = 0.0136

Figure 2

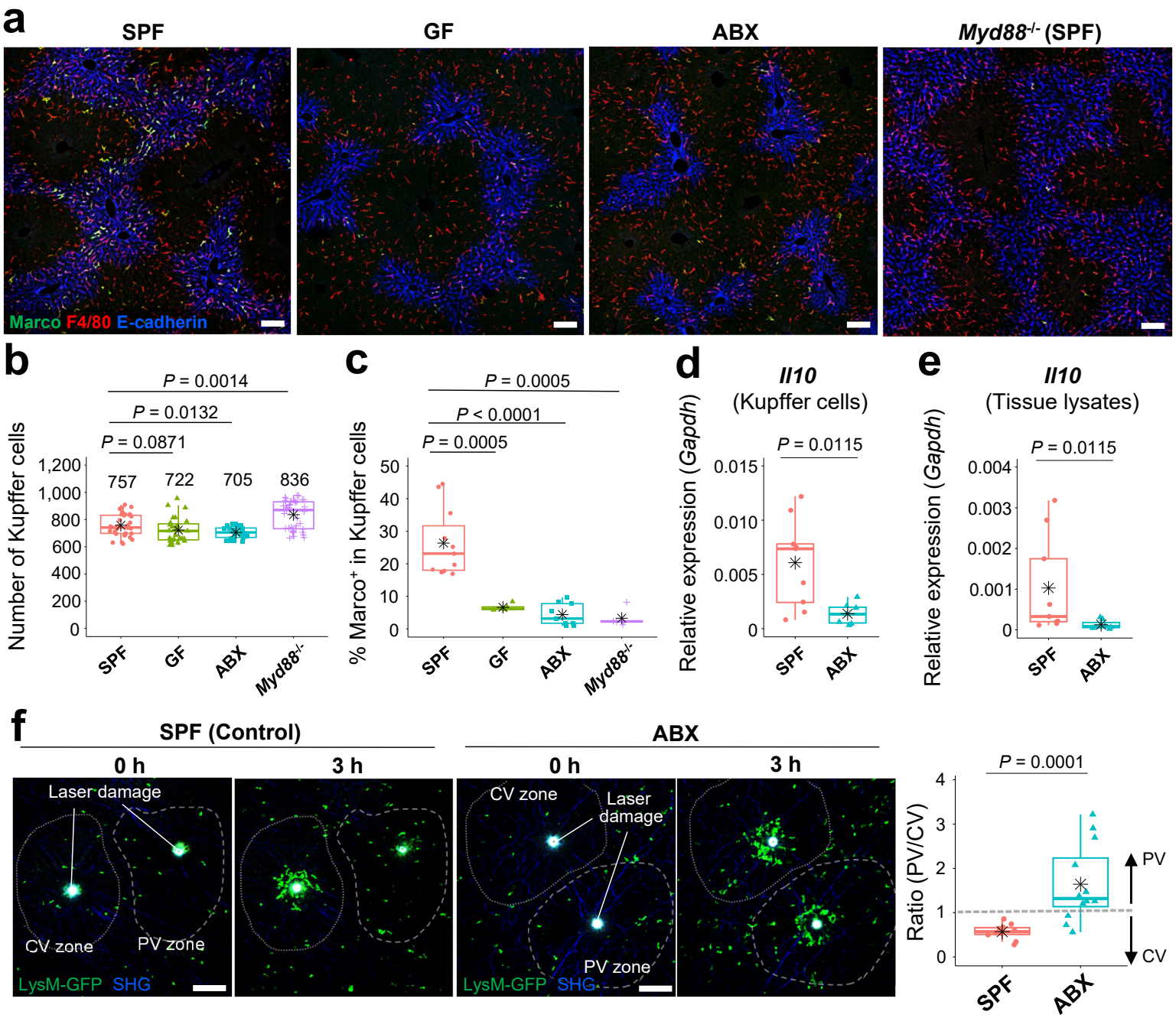
a
SPF
GF
ABX
Myd88-/- (SPF)
Marco F4/80 E-cadherin
b
Number of Kupffer cells
P = 0.0014
P = 0.0132
P = 0.0871
757
722
705
836
SPF
GF
ABX
Myd88-/-
c
% Marco+ in Kupffer cells
P = 0.0005
P < 0.0001
P = 0.0005
d
Il10
(Kupffer cells)
Relative expression (Gapdh)
P = 0.0115
e
Il10
(Tissue lysates)
Relative expression (Gapdh)
P = 0.0115
f
SPF (Control)
ABX
0 h
3 h
Laser damage
CV zone
PV zone
LysM-GFP SHG
Ratio (PV/CV)
P = 0.0001
PV
CV

Figure 3

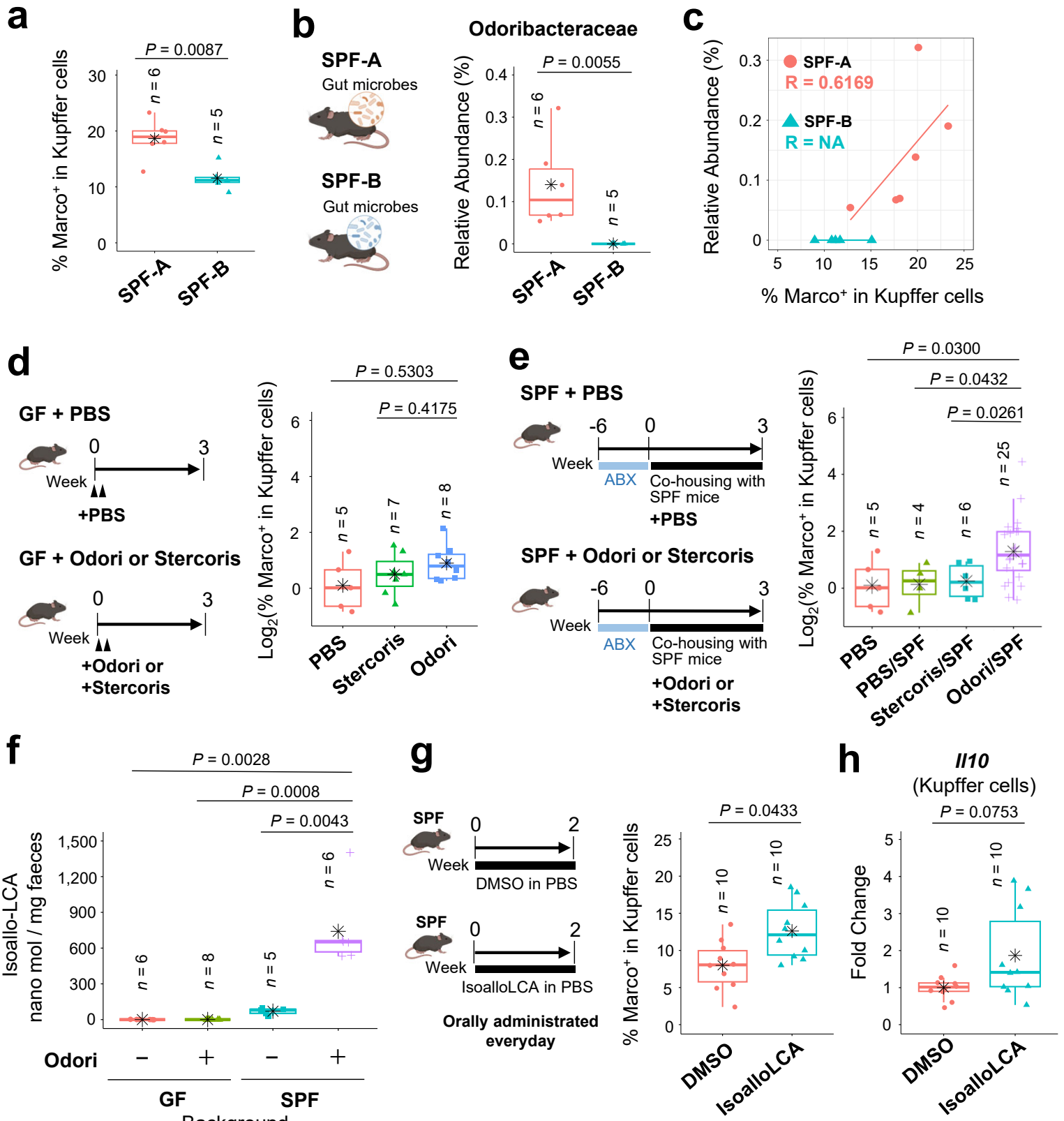
a
P = 0.0087
% Marco⁺ in Kupffer cells
n = 6
n = 5
SPF-A
SPF-B
b
SPF-A
Gut microbes
SPF-B
Gut microbes
Odoribacteraceae
P = 0.0055
Relative Abundance (%)
c
SPF-A
R = 0.6169
SPF-B
R = NA
Relative Abundance (%)
% Marco⁺ in Kupffer cells
d
GF + PBS
Week
+PBS
GF + Odori or Stercoris
+Odori or
+Stercoris
P = 0.5303
P = 0.4175
Log2(% Marco⁺ in Kupffer cells)
n = 5
n = 7
n = 8
PBS
Stercoris
Odori
e
SPF + PBS
ABX
Co-housing with
SPF mice
+PBS
SPF + Odori or Stercoris
+Odori or
+Stercoris
P = 0.0300
P = 0.0432
P = 0.0261
Log2(% Marco⁺ in Kupffer cells)
n = 5
n = 4
n = 6
n = 25
PBS
PBS/SPF
Stercoris/SPF
Odori/SPF
f
P = 0.0028
P = 0.0008
P = 0.0043
Isoallo-LCA
nano mol / mg faeces
n = 6
n = 8
n = 5
n = 6
Odori
GF
SPF
Background
g
SPF
Week
DMSO in PBS
IsoalloLCA in PBS
Orally administrated
everyday
P = 0.0433
% Marco⁺ in Kupffer cells
n = 10
n = 10
DMSO
IsoalloLCA
h
Il10
(Kupffer cells)
P = 0.0753
Fold Change
n = 10
n = 10
DMSO
IsoalloLCA

Figure 4

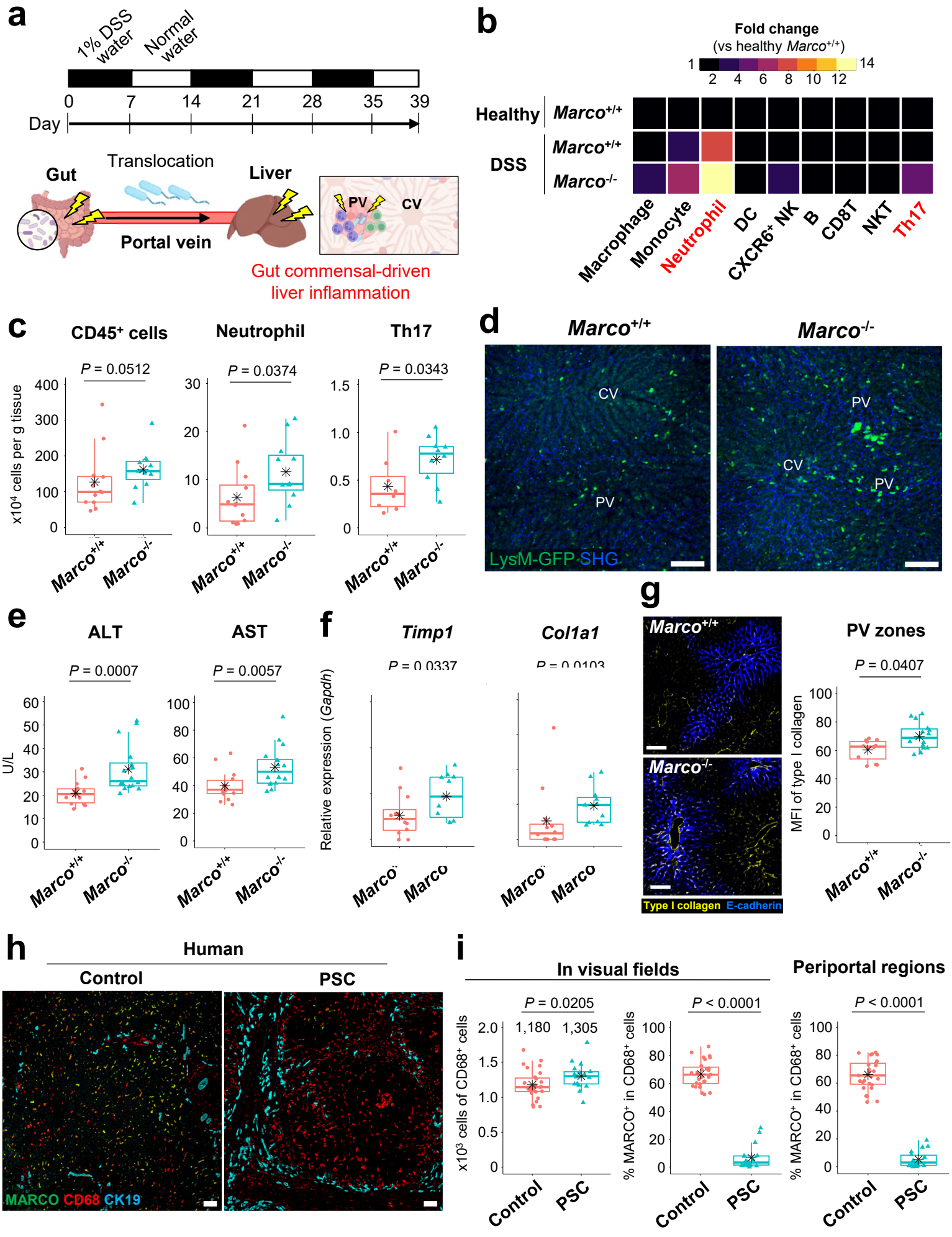
a
1% DSS water
Normal water
0
7
14
21
28
35
39
Day
Translocation
Gut
Liver
Portal vein
PV
CV
Gut commensal-driven liver inflammation
b
Fold change
(vs healthy Marco+/+)
1
2
4
6
8
10
12
14
Healthy
Marco+/+
DSS
Marco+/+
Marco-/-
Macrophage
Monocyte
Neutrophil
DC
CXCR6+ NK
B
CD8T
NKT
Th17
c
CD45+ cells
Neutrophil
Th17
P = 0.0512
P = 0.0374
P = 0.0343
x10⁴ cells per g tissue
Marco+/+
Marco-/-
d
Marco+/+
Marco-/-
CV
PV
LysM-GFP SHG
e
ALT
AST
P = 0.0007
P = 0.0057
U/L
f
Timp1
Col1a1
Relative expression (Gapdh)
g
Marco+/+
Marco-/-
Type I collagen E-cadherin
PV zones
P = 0.0407
MFI of type I collagen
h
Human
Control
PSC
MARCO CD68 CK19
i
In visual fields
Periportal regions
P = 0.0205
P < 0.0001
P < 0.0001
1,180
1,305
x10³ cells of CD68+ cells
% MARCO+ in CD68+ cells
Control
PSC

Figure 5